

ET**RAJ.JL:**

Trajectory-Based Simulation for Strong-Field Ionization

Mingyu Zhu,¹ Hongcheng Ni,^{1,2,3,*} and Jian Wu^{1,2,3,4}

¹*State Key Laboratory of Precision Spectroscopy, East China Normal University, Shanghai 200241, China*

²*NYU-ECNU Joint Institute of Physics, New York University at Shanghai, Shanghai 200062, China*

³*Collaborative Innovation Center of Extreme Optics, Shanxi University, Taiyuan, Shanxi 030006, China*

⁴*Chongqing Key Laboratory of Precision Optics, Chongqing Institute of East China Normal University, Chongqing 401121, China*

(Dated: November 2, 2024)

The dynamics of light-matter interactions in the realm of strong-field ionization has been a focal point and has attracted widespread interest. We present the `eTraj.jl` program package, designed to implement established classical/semiclassical trajectory-based methods to determine the photoelectron momentum distribution resulting from strong-field ionization of both atoms and molecules. The program operates within a unified theoretical framework that separates the trajectory-based computation into two stages: initial-condition preparation and trajectory evolution. For initial-condition preparation, we provide several methods, including the Strong-Field Approximation with Saddle-Point Approximation (SFA-SPA), SFA-SPA with Non-adiabatic Expansion (SFA-SPANE), and the Ammosov-Delone-Krainov theory (ADK), with atomic and molecular variants, as well as the Weak-Field Asymptotic Theory (WFAT) for molecules. For trajectory evolution, available options are Classical Trajectory Monte-Carlo (CTMC), which employs purely classical electron trajectories, and the Quantum Trajectory Monte-Carlo (QTMC) and Semi-Classical Two-Step model (SCTS), which include the quantum phase during trajectory evolution. The program is a versatile, efficient, and out-of-the-box solution for trajectory-based simulations for strong-field ionization. It is designed with user-friendliness in mind and is expected to serve as a valuable and powerful tool for the community of strong-field physics.

PROGRAM SUMMARY:

Program title: `eTraj.jl`

Repository link: <https://github.com/TheStarAlight/eTraj.jl>

Licensing provisions: Apache License, 2.0 (Apache-2.0)

Programming language: Julia

Platform: Linux (full functionality), macOS (full functionality), Windows (molecular calculation is restricted)

Nature of problem: Atoms and molecules exposed in an intense laser field go through complex processes of ionization through mechanisms such as multi-photon ionization and tunneling ionization. The trajectory-based methods are powerful tools for simulating these processes, and have considerable advantages over the time-dependent Schrödinger equation (TDSE) and the strong-field approximation (SFA). However, the community lacks a unified theoretical framework for trajectory-based methods, and there are no public-available code that implements the schemes.

Solution method: We developed a general, efficient, and out-of-the-box solution for trajectory-based simulation program named after `eTraj.jl` using the Julia programming language. The program is written in a clear and concise manner, and features versatility, extensibility, and usability.

* hcn@lps.ecnu.edu.cn

CONTENTS

I. Introduction	3
II. Theoretical Framework	4
A. Initial Conditions	4
1. Strong-Field Approximation with Saddle-Point Approximation (SFA-SPA)	4
2. SFA-SPA with Non-adiabatic Expansion (SFA-SPANE)	7
3. Ammosov-Delone-Krainov (ADK)	8
4. Molecular SFA-SPA/SFA-SPANE/ADK	9
5. Weak-Field Asymptotic Theory (WFAT)	9
B. Trajectory Simulation and Quantum Phase	11
1. Classical Trajectory Monte-Carlo (CTMC)	12
2. Quantum Trajectory Monte-Carlo (QTMC)	12
3. Semiclassical Two-Steps (SCTS) Model	13
III. Program Structure and Manual	15
A. Lasers Module	15
B. Targets Module	17
C. Electron Sampling and Trajectory Simulation	20
IV. Illustrative Examples	23
A. Attoclock Experiment and the Influence of Initial Condition Methods	23
B. Interaction with Linearly-polarized Pulses and the Influence of Quantum Phase	24
C. Interaction with an $\omega - 2\omega$ Bichromatic Clover-shaped Laser	26
D. WFAT-CTMC Simulation of Molecular Targets	27
V. Conclusions and Prospects	32
A. Ionization Rate of SFA-SPA in the Adiabatic Limit and the Coulomb-correction Term	33
Acknowledgments	34
References	34

I. INTRODUCTION

The interaction between light and matter has attracted widespread interest since the early days of quantum mechanics. With the advent of laser technology, the intensity of light and the precision of spectroscopy has dramatically increased, which allows us to explore the physics of light-matter interaction under extreme conditions with unprecedented precision and accuracy [1–3]. At a high laser intensity above TW/cm^2 , the interaction between light and atoms or molecules can no longer be described by the perturbation theory and a series of novel strong-field phenomena emerges, such as the above-threshold ionization (ATI) [4–6], tunneling ionization [7–11], high-harmonic generation (HHG) [12–17] and non-sequential double ionization (NSDI) [18, 19].

Theoretical studies of these non-perturbative phenomena have been extensively investigated in the past decades. Usually, in order to obtain a precise result, a time-dependent Schrödinger equation (TDSE) is solved numerically [20–24]. However, solving the TDSE is computationally expensive and resource-demanding, which limits its application to few-dimensional problems. Moreover, the TDSE is like a black box, offering limited transparency for interpreting the underlying physics. Apart from TDSE, the strong-field approximation (SFA) [7, 25–27] is also widely applied to study these problems, which is based on the assumptions that: (1) the initial state is not affected by the laser field until ionization; (2) after ionization, the photoelectron is not influenced by the trapping potential (i.e., assuming a short-range potential). These two approximations simplify the problem, which allows one to obtain analytical results and unravel the physical pictures of these phenomena. However, such approximations are not always applicable, especially when the Coulomb potential’s role becomes significant, which may lead to incorrect predictions [28–35].

To address these limitations, the scheme of *Classical-Trajectory Monte-Carlo* (CTMC) method [36, 37] can be adopted, where a microcanonical ensemble of classical electrons is prepared and evolved under the laser interaction or charged-particle impact. This scheme has been further developed to account for the initial stage of tunneling ionization by setting the initial conditions of the classical electrons at the tunnel exit [6, 15, 38]. The final photoelectron momentum distribution (PMD) is obtained through statistical analysis of the electron trajectories. While CTMC relies on purely classical electron trajectories, quantum effects can be largely retained by incorporating a phase into the electron trajectories. Examples include the *Trajectory-based Coulomb-SFA* (TC-SFA) [39, 40], the *Quantum-Trajectory Monte Carlo* (QTMC) [41–44], and the *Semiclassical Two-Step Model* (SCTS) [45–50]. Another approach, the *Coulomb Quantum-orbit SFA* (CQSFA) [51–56], addresses the inverse problem by identifying all trajectories that result in the same final momenta. These trajectory-based semiclassical methods offer notable advantages over the TDSE and direct SFA methods due to their lower demand on computational resources, as well as the clarity they provide in understanding the physical picture.

After years of development, various trajectory-based classical/semiclassical methods have emerged, yet a unified theoretical framework remains to be established. Besides, developing a library that implements existing methods, which is efficient in calculations and is easy to maintain, would greatly facilitate further research on strong-field ionization. With this goal in mind, we introduce `eTraj.jl`, a program package written in the Julia language, which provides a general, efficient, and out-of-the-box solution for performing classical/semiclassical trajectory simulations. This library is written in a clear and concise manner, ensuring versatility, extensibility, and usability.

This article is organized as follows. In Sec. II, we introduce the theoretical framework of `eTraj`, covering the commonly-used initial condition and phase methods in the trajectory-based approaches. In Sec. III, we detail the structure and manual of `eTraj` in detail. In Sec. IV, we present several illustrative examples to demonstrate the practical applications of `eTraj`. Sec. V concludes this article. Atomic units (a.u.) are used in this article unless stated otherwise.

II. THEORETICAL FRAMEWORK

A. Initial Conditions

Several theories on strong-field ionization can be utilized to prepare the initial conditions of the classical electrons in the trajectory simulation scheme. The initial condition consists of three properties:

- Initial position \mathbf{r}_0 , i.e., the tunneling exit position;
- Initial momentum \mathbf{k}_0 [57];
- The corresponding ionization probability W carried by each electron sample, which depends on the time-dependent laser field and properties of the target atom/molecule.

In this section we briefly revisit the available theories [3] implemented in `eTraj`.

1. Strong-Field Approximation with Saddle-Point Approximation (SFA-SPA)

The *Strong-Field Approximation (SFA)* is originated from the Keldysh theory of strong-field ionization [7, 25–27]. Compared with the perturbative methods and adiabatic tunneling theories, the SFA is applicable to both the multi-photon and the tunneling processes during the laser-atom interaction, because it fully includes the non-adiabatic effect of the laser-atom interaction. The broad scope of SFA has contributed to its widespread application in theoretical investigations of strong-field ionization.

We consider an electron evolving under a combined field of the Coulomb field $V(\mathbf{r})$ of the parent ion and the laser field $\mathbf{F}(t) = -\partial_t \mathbf{A}(t)$, where $\mathbf{F}(t)$ and $\mathbf{A}(t)$ are the electric field and vector potential of the laser field, respectively. Under the length gauge (LG), its Hamiltonian reads

$$H^{\text{LG}} = \frac{1}{2} \mathbf{p}^2 + V(\mathbf{r}) + \mathbf{F}(t) \cdot \mathbf{r}. \quad (1)$$

Denoting $|\Psi_0\rangle = |\psi_0\rangle e^{iI_p t}$ as the unperturbed initial state with ionization potential of I_p , $|\Psi_{\mathbf{p}}\rangle$ as the continuum state of momentum \mathbf{p} , and

$$U(t_f, t_0) = \exp \left[-i \int_{t_0}^{t_f} H^{\text{LG}}(\tau) d\tau \right] \quad (2)$$

the time-evolution operator, the transition amplitude between the initial state (at t_0) and the final state of momentum \mathbf{p} (at t_f) is written as

$$M_{\mathbf{p}} = \langle \Psi_{\mathbf{p}} | U(t_f, t_0) | \Psi_0 \rangle. \quad (3)$$

Here lies the key idea of SFA: when the influence of the Coulomb field to the ionized electrons is weak compared with that of the external laser field, we may neglect the influence of the Coulomb field in the expression of $M_{\mathbf{p}}$ by replacing the time-evolution operator with a Coulomb-free one U_f , and meanwhile replacing the continuum state with the Volkov state $|\Psi_{\mathbf{p}}^V\rangle$ which represents a free electron evolving under the same laser field:

$$M_{\mathbf{p}} \approx \langle \Psi_{\mathbf{p}}^V | U_f(t_f, t_0) | \Psi_0 \rangle, \quad (4)$$

where the Volkov state under the LG is the product of a plane wave and a phase factor:

$$|\Psi_{\mathbf{p}}^V\rangle = |\mathbf{p} + \mathbf{A}(t)\rangle \exp \left\{ -i \int^t \frac{1}{2} [\mathbf{p} + \mathbf{A}(\tau)]^2 d\tau \right\}. \quad (5)$$

In this way the $M_{\mathbf{p}}$ is expressed as

$$M_{\mathbf{p}} = -i \int_{t_0}^{t_f} \langle \mathbf{p} + \mathbf{A}(\tau) | \mathbf{F}(\tau) \cdot \mathbf{r} | \psi_0 \rangle e^{-iS_{\mathbf{p}}(\tau)} d\tau, \quad (6)$$

and we note that here we have extracted the phase factor of $|\Psi_0\rangle$ and combined it with that of the Volkov state $|\Psi_{\mathbf{p}}^V\rangle$, giving the phase

$$S_{\mathbf{p}}(t) = - \int^t \left\{ \frac{1}{2} [\mathbf{p} + \mathbf{A}(\tau)]^2 + I_p \right\} d\tau. \quad (7)$$

Inserting

$$\frac{\partial}{\partial t} \langle \mathbf{p} + \mathbf{A}(t) | = i \langle \mathbf{p} + \mathbf{A}(t) | [\mathbf{F}(t) \cdot \mathbf{r}] \quad (8)$$

into the above expression of $M_{\mathbf{p}}$ [Eq. (6)], after integration by parts, one obtains

$$\begin{aligned} M_{\mathbf{p}} &= - \int_{t_0}^{t_f} d\tau \frac{\partial}{\partial \tau} [\langle \mathbf{p} + \mathbf{A}(\tau) | \psi_0 \rangle] e^{-iS_{\mathbf{p}}(\tau)} \\ &= - \langle \mathbf{p} + \mathbf{A}(\tau) | \psi_0 \rangle e^{-iS_{\mathbf{p}}(\tau)} \Big|_{t_0}^{t_f} + \int_{t_0}^{t_f} d\tau \langle \mathbf{p} + \mathbf{A}(\tau) | \psi_0 \rangle \cdot [-iS'_{\mathbf{p}}(\tau)] e^{-iS_{\mathbf{p}}(\tau)}. \end{aligned} \quad (9)$$

An additional saddle-point approximation (SPA) facilitates preparation of initial conditions of the electron trajectories. The variation of phase factor $e^{iS_{\mathbf{p}}(t)}$ is much more sensitive than that of the prefactor as t varies, which leads to the fact that the whole integrand in Eq. (9) oscillates in its complex phase and its values cancel out in most cases, except when the variation of the phase $S_{\mathbf{p}}(t)$ becomes stable, i.e., at the saddle points. The saddle points $t_s = t_r + it_i$ are the zeroes of the derivative of the complex function $S_{\mathbf{p}}(t)$, which satisfy

$$-S'_{\mathbf{p}}(t_s) = \frac{1}{2} [\mathbf{p} + \mathbf{A}(t_s)]^2 + I_p = 0. \quad (10)$$

The second term of the r.h.s. of Eq. (9), i.e., the integral, has significant contribution only in the vicinity of the two end points t_0, t_f and the saddle points t_s , while the contribution near the two end points cancels out the first term. Therefore, the $M_{\mathbf{p}}$ is now approximated with the integration around the saddle points:

$$M_{\mathbf{p}} \approx \sum_{t_s} \int_{C_{t_s}} d\tau \langle \mathbf{p} + \mathbf{A}(\tau) | \psi_0 \rangle \cdot [-iS'_{\mathbf{p}}(\tau)] e^{-iS_{\mathbf{p}}(\tau)}, \quad (11)$$

with C_{t_s} the integration contour following the steepest-descent path related to t_s .

Further evaluation of the prefactor $\tilde{\psi}_0(\mathbf{k})|_{\mathbf{k}=\mathbf{p}+\mathbf{A}(t)} = \langle \mathbf{p} + \mathbf{A}(t) | \psi_0 \rangle$ (i.e., the momentum-space wavefunction) in the vicinity of the saddle points in Eq. (11) is essential before applying the SPA. We assume the field points towards the $+z$ axis, for an atom target at the (l, m) state with ionization potential I_p , its wavefunction behaves asymptotically as [58]

$$\psi_0(\mathbf{r}) \sim 2C_{\kappa l} \kappa^{3/2} (\kappa r)^{n^*-1} e^{-\kappa r} Y_{lm}(\hat{\mathbf{r}}) \quad (12)$$

for $\kappa r \gg 1$, with $\kappa = \sqrt{2I_p}$, $n^* = Z/\kappa$ the effective principal quantum number, Z the charge of the residual ion, Y_{lm} the spherical harmonics, and $C_{\kappa l}$ the asymptotic coefficient for atoms, which can be approximated using the Hartree approximation formula [59]

$$C_{\kappa l}^2 = \frac{2^{2n^*-2}}{n^*(n^*+l)!(n^*-l-1)!}. \quad (13)$$

For atomic hydrogen at the ground state we have $C_{\kappa l} = 1$. Moreover, for non-integer n^* , the formula can be naturally extended by replacing the factorials $x!$ with Gamma functions $\Gamma(x+1)$, i.e.,

$$C_{\kappa l}^2 = \frac{2^{2n^*-2}}{n^* \Gamma(n^*+l+1) \Gamma(n^*-l)}. \quad (14)$$

In the vicinity of the saddle points, which corresponds to the case when $k^2 \rightarrow -\kappa^2$, the expression of $\tilde{\psi}_0(\mathbf{k})$ is determined by the asymptotic behavior of the wavefunction [60]:

$$\tilde{\psi}_0(\mathbf{k}) = \frac{C_{\kappa l}}{\sqrt{\pi}} \frac{2^{n^*+3/2} \kappa^{2n^*+1/2} \Gamma(n^*+1)}{(k^2 + \kappa^2)^{n^*+1}} Y_{lm}(\hat{\mathbf{k}}). \quad (15)$$

Substituting the above expression into Eq. (11), making use of the definition of $S_{\mathbf{p}}(t)$ [Eq. (7)], we obtain

$$M_{\mathbf{p}} = i \frac{C_{\kappa l}}{\sqrt{\pi}} 2^{1/2} \kappa^{2n^*+1/2} \Gamma(n^*+1) \sum_{t_s} \int_{C_{t_s}} \frac{Y_{lm}[\hat{\mathbf{k}}(\tau)]}{[S'_{\mathbf{p}}(\tau)]^{n^*}} e^{iS_{\mathbf{p}}(\tau)} d\tau, \quad (16)$$

where $\hat{\mathbf{k}}(\tau)$ is the complex unit vector along $\mathbf{k}(\tau) = \mathbf{p} + \mathbf{A}(\tau)$, and the evaluation method of spherical harmonics with complex arguments is based on Appendix B of Ref. [61], see also note [62]. A modified version of SPA can be carried out to handle the case when the integrand has a singularity at t_s (see Appendix B of Ref. [63]):

$$\begin{aligned} \int_{C_{t_s}} \frac{Y_{lm}[\hat{\mathbf{k}}(\tau)]}{[S'_{\mathbf{p}}(\tau)]^{n^*}} e^{iS_{\mathbf{p}}(\tau)} d\tau &\approx \frac{Y_{lm}[\hat{\mathbf{k}}(t_s)]}{[S''_{\mathbf{p}}(t_s)]^{n^*}} \int_{C_{t_s}} \frac{e^{iS_{\mathbf{p}}(\tau)}}{(\tau - t_s)^{n^*}} d\tau \\ &\approx \frac{Y_{lm}[\hat{\mathbf{k}}(t_s)]}{[S''_{\mathbf{p}}(t_s)]^{n^*}} \cdot i^{n^*} \frac{\Gamma(n^*/2)}{2\Gamma(n^*)} \sqrt{\frac{2\pi}{-iS''_{\mathbf{p}}(t_s)}} [-2iS''_{\mathbf{p}}(t_s)]^{n^*/2} e^{iS_{\mathbf{p}}(t_s)}. \end{aligned} \quad (17)$$

In this way we find the expression of the transition amplitude:

$$M_{\mathbf{p}} = c_{n^*} C_{\kappa l} \sum_{t_s} \frac{Y_{lm}[\hat{\mathbf{k}}(t_s)]}{[S''_{\mathbf{p}}(t_s)]^{(n^*+1)/2}} e^{-iS_{\mathbf{p}}(t_s)}, \quad (18)$$

with $c_{n^*} = i^{(n^*-5)/2} 2^{n^*/2+1} \kappa^{2n^*+1/2} \Gamma(n^*/2+1)$ the constant coefficient.

The SFA phase $S_{\mathbf{p}}(t_s)$ is obtained by solving the integral

$$\begin{aligned} S_{\mathbf{p}}(t_s) &= - \int_{t_s}^{\infty} d\tau \left\{ \frac{1}{2} [\mathbf{p} + \mathbf{A}(\tau)]^2 + I_p \right\} \\ &= \left(- \int_{t_s}^{t_r} - \int_{t_r}^{\infty} \right) d\tau \left\{ \frac{1}{2} [\mathbf{p} + \mathbf{A}(\tau)]^2 + I_p \right\} \\ &= S_{\mathbf{p},\text{tun}} + S_{\mathbf{p},\text{traj}}, \end{aligned} \quad (19)$$

where the terms $S_{\mathbf{p},\text{tun}}$ and $S_{\mathbf{p},\text{traj}}$ represent the complex phases accumulated during the tunneling process and the trajectory motion in the continuum, respectively. The phase $S_{\mathbf{p},\text{tun}}$ is accumulated during an imaginary period of time (from time t_s to t_r), in which the electron passes through the potential barrier with an ‘imaginary’ momentum, its real part denotes the quantum phase, while its imaginary part is related to the ionization probability.

To utilize the SFA to prepare initial conditions of the photoelectrons, we suppose that the electron is released at time t_r at the tunnel exit \mathbf{r}_0 with momentum $\mathbf{k}_0 = \mathbf{k}(t_r)$. The initial momentum \mathbf{k}_0 , neglecting the Coulomb interaction with the nucleus, is related to the final momentum \mathbf{p} through

$$\mathbf{p} = \mathbf{k}_0 - \int_{t_r}^{\infty} \mathbf{F}(\tau) d\tau = \mathbf{k}_0 - \mathbf{A}(t_r). \quad (20)$$

The initial position \mathbf{r}_0 , i.e., the tunnel exit, is found by constructing a quantum tunneling trajectory. The beginning of the trajectory, i.e., the tunnel entrance, has a vanishing real part; the electron tunnels through the barrier during the time interval t_s to t_r and emerges as a classical electron at the tunnel exit \mathbf{r}_0 with a real position and momentum. In this way we obtain the expression of the initial position:

$$\mathbf{r}_0^{\text{SFA-SPA}} = \Re \int_{t_s}^{t_r} [\mathbf{p} + \mathbf{A}(\tau)] d\tau = \Im \int_0^{t_i} \mathbf{A}(t_r + i\tau) d\tau, \quad (21)$$

where \Re and \Im are the real and imaginary part notation, respectively.

The probability density (in the final momentum space \mathbf{p}) carried by the electron sample is

$$dW^{\text{SFA-SPA}}/d\mathbf{p} = \sum_{t_s} |\mathcal{P}_{\mathbf{p}}^{\text{SFA-SPA}}(t_s)|^2 \exp\{-2\Im S_{\mathbf{p},\text{tun}}(t_s)\}, \quad (22)$$

where we have gathered the coefficients to the prefactor

$$\mathcal{P}_{\mathbf{p}}^{\text{SFA-SPA}}(t_s) = c_{n^*} \frac{C_{\kappa l} Y_{lm}[\hat{\mathbf{k}}(t_s)]}{[S_{\mathbf{p}}''(t_s)]^{(n^*+1)/2}} = c_{n^*} \frac{C_{\kappa l} Y_{lm}[\hat{\mathbf{k}}(t_s)]}{\{[\mathbf{p} + \mathbf{A}(t_s)] \cdot \mathbf{F}(t_s)\}^{(n^*+1)/2}}. \quad (23)$$

We note that the ionization probability in Eq. (22) is expressed in the coordinate of the final momentum $\mathbf{p} = (p_x, p_y, p_z)$. However, in the trajectory simulation, the initial electrons are sampled in the (t_r, \mathbf{k}_t) coordinate, with \mathbf{k}_t the initial transversal momentum. Thus, adding a Jacobian in the prefix of the ionization probability is required if we sample the initial electrons within such a coordinate. Suppose the laser propagates in the z axis and polarizes in the xy plane, the transformed expression reads

$$dW^{\text{SFA-SPA}}/dt_r d\mathbf{k}_t = \sum_{t_s} J(t_r, k_{\perp}) |\mathcal{P}_{\mathbf{p}}^{\text{SFA-SPA}}(t_s)|^2 \exp(-2\Im S_{\mathbf{p},\text{tun}}(t_s)), \quad (24)$$

where k_{\perp} is the projection of \mathbf{k}_t on the polarization plane (i.e., the xy plane), and the Jacobian is

$$J(t_r, k_{\perp}) = \left| \frac{\partial(p_x, p_y)}{\partial(t_r, k_{\perp})} \right| = \left| \frac{\partial p_x / \partial t_r \quad \partial p_x / \partial k_{\perp}}{\partial p_y / \partial t_r \quad \partial p_y / \partial k_{\perp}} \right|. \quad (25)$$

2. SFA-SPA with Non-adiabatic Expansion (SFA-SPANE)

For a small Keldysh parameter $\gamma = \omega\kappa/F_0$ (ω is the laser angular frequency and F_0 is the peak field strength), the non-adiabatic effect is not significant, thus a non-adiabatic expansion scheme can be carried out to develop an approximate theory based on the SFA-SPA, which is named after the *SFA-SPA with Non-adiabatic Expansion (SFA-SPANE)* [3, 64–68]. It includes the non-adiabatic effect to a large extent and is capable of giving similar results compared with that given by the SFA-SPA under relatively small Keldysh parameters. SFA-SPANE comes with a closed analytical form, avoiding the necessity to solve the saddle-point equation, thereby speeding up the calculation.

The SFA-SPANE method is applicable when the Keldysh parameter is small, and the non-adiabatic effect is insignificant, which corresponds to the small- t_i case. We expand the vector potential $\mathbf{A}(t_s) = \mathbf{A}(t_r + it_i)$ in the SFA-SPA around $t_i = 0$, up to the second order of t_i :

$$\mathbf{A}(t_r + it_i) = \mathbf{A}(t_r) - it_i \mathbf{F}(t_r) + \frac{1}{2} t_i^2 \mathbf{F}'(t_r) + o(t_i^2). \quad (26)$$

Inserting Eq. (26) into the saddle-point equation in the SFA-SPA [Eq. (10)] leads to

$$\mathbf{k}(t_r) \cdot \mathbf{F}(t_r) \approx 0 \quad (27)$$

and

$$t_i \approx \sqrt{\frac{k^2(t_r) + \kappa^2}{F^2(t_r) - \mathbf{k}(t_r) \cdot \mathbf{F}'(t_r)}}, \quad (28)$$

which allow for the derivation of analytical expressions of the ionization probability and other quantities.

The initial position \mathbf{r}_0 in SFA-SPANE, is given by

$$\mathbf{r}_0^{\text{SFA-SPANE}} = \Im \int_0^{t_i} \mathbf{A}(t_r + i\tau) d\tau = -\frac{\mathbf{F}}{2} \frac{k_t^2 + \kappa^2}{F^2 - \mathbf{k}_0 \cdot \mathbf{F}'}. \quad (29)$$

The $\mathfrak{S}S_{\mathbf{p},\text{tun}}$ term, which is related to the ionization probability, in the SFA-SPANE, is

$$\begin{aligned}\mathfrak{S}S_{\mathbf{p},\text{tun}} &\approx \mathfrak{S} \int_{t_r}^{t_s} d\tau \left\{ \frac{1}{2} \left[\mathbf{p} + \mathbf{A}(t_r) - it_i \mathbf{F}(t_r) + \frac{1}{2} t_i^2 \mathbf{F}'(t_r) \right]^2 + I_p \right\} \\ &\approx \left[I_p + \frac{1}{2} k^2(t_r) \right] t_i - [F^2(t_r) - \mathbf{k}(t_r) \cdot \mathbf{F}'(t_r)] \frac{t_i^3}{6} \\ &= \frac{1}{3} \frac{(k^2 + \kappa^2)^{3/2}}{\sqrt{F^2 - \mathbf{k}_0 \cdot \mathbf{F}'}}.\end{aligned}\quad (30)$$

Then follows the ionization probability

$$dW^{\text{SFA-SPANE}}/d\mathbf{p} = |\mathcal{P}_{\mathbf{p}}^{\text{SFA-SPANE}}(t_s)|^2 \exp \left[-\frac{2}{3} \frac{(k_t^2 + \kappa^2)^{3/2}}{\sqrt{F^2 - \mathbf{k}_0 \cdot \mathbf{F}'}} \right], \quad (31)$$

where \mathbf{k}_t is actually equivalent to $\mathbf{k}(t_r)$ in the SFA-SPANE because of the vanishing initial longitudinal momentum as in Eq. (27). The prefactor reads

$$\mathcal{P}_{\mathbf{p}}^{\text{SFA-SPANE}}(t_s) = c_{n^*} \frac{C_{\kappa l} Y_{lm}[\hat{\mathbf{k}}(t_s)]}{[(k_t^2 + \kappa^2)(F^2 - \mathbf{k}_0 \cdot \mathbf{F}')]^{(n^*+1)/4}}. \quad (32)$$

3. Ammosov-Delone-Krainov (ADK)

The *Ammosov-Delone-Krainov (ADK)* theory [8, 9] is used to study the scenario of adiabatic tunneling in strong-field ionization, and is, in a sense, the adiabatic limit of the SFA.

In the adiabatic limit, the laser field can be treated as static, thus we have $\mathbf{F}'(t) = 0$ [higher order derivatives of $\mathbf{F}(t)$ remains zero as well]. Substituting it into the ionization probability of SFA-SPANE [Eq. (31)] gives

$$dW^{\text{ADK}}/d\mathbf{p} = |\mathcal{P}_{\mathbf{p}}^{\text{ADK}}(t_s)|^2 \exp \left[-\frac{2}{3} \frac{(k_t^2 + \kappa^2)^{3/2}}{F} \right], \quad (33)$$

where the prefactor reads

$$\mathcal{P}_{\mathbf{p}}^{\text{ADK}}(t_s) = c_{n^*} \frac{C_{\kappa l} Y_{lm}[\hat{\mathbf{k}}(t_s)]}{[(k_t^2 + \kappa^2)F^2]^{(n^*+1)/4}}, \quad (34)$$

with $t_i = \sqrt{k_t^2 + \kappa^2}/F$. If we expand Eq. (33) under the small- k_t limit, we obtain

$$dW^{\text{ADK}}/d\mathbf{p} \propto \exp \left(-\frac{2\kappa^3}{3F} \right) \exp \left(-\frac{\kappa k_t^2}{F} \right), \quad (35)$$

which is actually the exponential term of the well-known ADK rate. However, we note that the result of our approach, i.e., applying the adiabatic limit of the SFA-SPA, is slightly different from the actual ADK rate in the prefactor. This is because the SFA framework neglects Coulomb potential in the final state, which has been shown to result in a lower ionization rate. As a remedy, introducing an additional Coulomb-correction (CC) factor [Eq. (A15)] to Eq. (33) bridges the gap:

$$C^{\text{CC}} = \left(\frac{2\kappa^3}{F} \right)^{n^*} (1 + 2\gamma/e)^{-2n^*} \left[\Gamma \left(\frac{n^*}{2} + 1 \right) \right]^{-2}. \quad (36)$$

We note that this CC factor is implemented in all initial-condition methods that are derived from the SFA. For more details, we refer the readers to Appendix A.

The tunnel exit is found with the same approach:

$$\mathbf{r}_0^{\text{ADK}} = \mathfrak{S} \int_0^{t_i} \mathbf{A}(t_r + i\tau) d\tau = -\frac{\mathbf{F}}{2} \frac{k_t^2 + \kappa^2}{F^2}, \quad (37)$$

which we refer to as the “ I_p/F ” model, but with a slight difference in that we have replaced the ionization potential $I_p = \kappa^2/2$ with the effective one $\tilde{I}_p = (\kappa^2 + k_t^2)/2$ to account for the initial kinetic energy, which ensures adiabatic tunneling: $E = k_t^2/2 + \mathbf{r}_0^{\text{ADK}} \cdot \mathbf{F} = -I_p$.

4. Molecular SFA-SPA/SFA-SPANE/ADK

The atomic SFA theory and its adiabatic versions mentioned in Sections II A 1 to II A 3 can be generalized naturally to molecular cases [69–72]. Under the Born-Oppenheimer [73] and the single-active-electron (SAE) approximation, the strong-field ionization of the molecules can be modeled as the interaction of the laser field and the ionizing orbital [often the highest occupied molecular orbital (HOMO)] $\psi_0(\mathbf{r})$ within the effective potential of the parent ion.

To generalize the atomic SFA to the molecular SFA (MO-SFA), we start from the transition amplitude in Eq. (11). In the molecular frame (MF), the asymptotic wavefunction can be expanded into spherical harmonics:

$$\psi_0^{\text{MF}}(\mathbf{r}) \sim \sum_{l,m} 2C_{lm} \kappa^{3/2} (\kappa r)^{n^*-1} e^{-\kappa r} Y_{lm}(\hat{\mathbf{r}}), \quad (38)$$

where the C_{lm} are asymptotic coefficients, and we continue to adopt the $n^* = Z/\kappa$ for simplicity, although it does not represent the effective principal quantum number anymore. We assume that in the field frame (FF) the field \mathbf{F} points towards the z axis, and the rotation $\hat{\mathbf{R}}$ from the FF to the MF can be defined via a set of Euler angles (ϕ, θ, χ) within the $z - y' - z''$ convention, which satisfies

$$\psi_0^{\text{MF}}(\hat{\mathbf{R}}\mathbf{r}) = \psi_0^{\text{FF}}(\mathbf{r}). \quad (39)$$

Utilizing the Wigner- D matrix, the rotated spherical harmonic function can be expressed as a linear combination of spherical harmonics of the same order l :

$$\hat{\mathbf{R}}(\phi, \theta, \chi) Y_{lm} = \sum_{m'} D_{m'm}^l(\phi, \theta, \chi) Y_{lm'} \quad (40)$$

and the asymptotic behavior of the wavefunction in the FF is found by inserting Eq. (40) into Eq. (38), which gives

$$\psi_0^{\text{FF}}(\mathbf{r}) \sim \sum_{l,m,m'} 2C_{lm} D_{m'm}^l(\phi, \theta, \chi) \kappa^{3/2} (\kappa r)^{n^*-1} e^{-\kappa r} Y_{lm'}(\hat{\mathbf{r}}). \quad (41)$$

It is obvious that the molecular version of the theory differs from the atomic one only in the expression of prefactor $\mathcal{P}_{\mathbf{p}}(t_s)$, while the expression of the tunneling exit position and the initial momentum are identical. Following the same procedure in Sec. II A 1 to II A 3, we obtain the prefactor $\mathcal{P}_{\mathbf{p}}$ that is applicable for molecules:

$$\mathcal{P}_{\mathbf{p}}^{\text{SFA-SPA}}(t_s) = c_{n^*} \frac{\sum_{l,m,m'} C_{lm} D_{m'm}^l(\phi, \theta, \chi) Y_{lm'}[\hat{\mathbf{k}}(t_s)]}{\{[\mathbf{p} + \mathbf{A}(t_s)] \cdot \mathbf{F}(t_s)\}^{(n^*+1)/2}}, \quad (42)$$

$$\mathcal{P}_{\mathbf{p}}^{\text{SFA-SPANE}}(t_s) = c_{n^*} \frac{\sum_{l,m,m'} C_{lm} D_{m'm}^l(\phi, \theta, \chi) Y_{lm'}[\hat{\mathbf{k}}(t_s)]}{[(k_t^2 + \kappa^2)(F^2 - \mathbf{k}_0 \cdot \mathbf{F}')]^{(n^*+1)/4}}, \quad (43)$$

$$\mathcal{P}_{\mathbf{p}}^{\text{ADK}}(t_s) = c_{n^*} \frac{\sum_{l,m,m'} C_{lm} D_{m'm}^l(\phi, \theta, \chi) Y_{lm'}[\hat{\mathbf{k}}(t_s)]}{[(k_t^2 + \kappa^2)F^2]^{(n^*+1)/4}}. \quad (44)$$

We also note that after applying an additional Coulomb-correction factor [Eq. (36)], the ionization rate aligns with the original MO-ADK theory [70] in the adiabatic and small- k_t limit.

5. Weak-Field Asymptotic Theory (WFAT)

The *Weak-Field Asymptotic Theory (WFAT)* generalizes the tunneling ionization from isotropic atomic potentials to arbitrary molecular potentials [74–82]. Compared with the MO-ADK theory, the WFAT naturally accounts for the influence of the permanent dipole moment of the molecule, and could, in its integral representation, calculate the structure factors

[a similar concept to the asymptotic coefficients C_{lm} in Eq. (38)] based on the wavefunction close to the core, rather than using the wavefunction in the asymptotic region, allowing for enhanced accuracy in numerical simulations.

The formulation of the WFAT is based on the expansion in the parabolic coordinates. The total ionization rate w , is split into different parabolic channels:

$$w^{\text{WFAT}} = \sum_{\nu} w_{\nu}, \quad (45)$$

where w_{ν} are partial rates of parabolic quantum number indices $\nu = (n_{\xi}, m)$ with $n_{\xi} = 0, 1, 2, \dots$ and $m = 0, \pm 1, \pm 2, \dots$. In the leading-order approximation of the WFAT, the partial rates can be separated into two factors, namely the structural part $|G_{\nu}(\theta, \chi)|^2$ and the field part $\mathcal{W}_{\nu}(F)$:

$$w_{\nu} = |G_{\nu}(\theta, \chi)|^2 \mathcal{W}_{\nu}(F). \quad (46)$$

The field factor is expressed as

$$\mathcal{W}_{\nu}(F) = \frac{\kappa}{2} \left(\frac{4\kappa^2}{F} \right)^{2n^* - 2n_{\xi} - |m| - 1} e^{-2\kappa^3/3F}. \quad (47)$$

The structure factor $G_{\nu}(\theta, \chi)$ is found by an integral related to the ionizing orbital and a reference function, which has significant contribution only in the vicinity of the nuclei and is insensitive to the wavefunction's asymptotic behavior:

$$G_{\nu}(\theta, \chi) = e^{-\kappa\mu_F} \int d\mathbf{r} \Omega_{\nu}^*(\hat{\mathbf{R}}^{-1}\mathbf{r}) \hat{V}_c \psi_0(\mathbf{r}), \quad (48)$$

which is evaluated in the MF, with $\psi_0(\mathbf{r})$ the wavefunction of the ionizing orbital;

$$\mu = - \int d\mathbf{r} \psi_0^*(\mathbf{r}) \mathbf{r} \psi_0(\mathbf{r}) \quad (49)$$

is the orbital dipole moment in the MF, with μ_F being its component along the field direction;

$$\Omega_{\nu}(\mathbf{r}) = \sum_{l=|m|}^{\infty} \Omega_{lm}^{\nu}(\mathbf{r}) = \sum_{l=|m|}^{\infty} R_l^{\nu}(r) Y_{lm}(\hat{\mathbf{r}}) \quad (50)$$

is a reference function which can be expanded into spherical harmonics, with its radial part expressed as

$$R_l^{\nu}(r) = \omega_l^{\nu} (\kappa r)^l e^{-\kappa r} M(l+1-n^*, 2l+2, 2\kappa r), \quad (51)$$

where $M(a, b, x)$ is the confluent hyper-geometric function and

$$\begin{aligned} \omega_l^{\nu} = & (-1)^{l+(|m|-m)/2+1} 2^{l+3/2} \kappa^{n^* - (|m|+1)/2 - n_{\xi}} \\ & \times \sqrt{(2l+1)(l+m)!(l-m)! (|m|+n_{\xi})! n_{\xi}!} \frac{l!}{(2l+1)!} \\ & \times \sum_{k=0}^{\min(n_{\xi}, l-|m|)} \frac{\Gamma(l+1-n^*+n_{\xi}-k)}{k!(l-k)! (|m|+k)! (l-|m|-k)! (n_{\xi}-k)!} \end{aligned} \quad (52)$$

is the normalization coefficient; $\hat{V}_c = \hat{V} + Z/r$ is the core potential with the Coulomb tail removed, where Z is the asymptotic charge of the residual ion.

The effective potential \hat{V} describes the interaction between the ionizing electron and the residual parent ion. We note that here we use the hat notation to indicate that the potential operator is not diagonal in the coordinate space. Under the framework of the Hartree-Fock method, the effective potential consists of three parts, namely the nuclear Coulomb potential (V_{nuc}), the direct (V_{d}) and exchange (V_{ex}) parts of inter-electron interactions:

$$\hat{V} = V_{\text{nuc}} + V_{\text{d}} + \hat{V}_{\text{ex}}, \quad (53)$$

with

$$\begin{aligned}
V_{\text{nuc}}(\mathbf{r}) &= - \sum_{A=1}^{N_{\text{atm}}} \frac{Z_A}{|\mathbf{r} - \mathbf{R}_A|}, \\
V_{\text{d}}(\mathbf{r}) &= \sum_{i=1}^N \int \frac{\psi_i^*(\mathbf{r}')\psi_i(\mathbf{r}')}{|\mathbf{r} - \mathbf{r}'|} d\mathbf{r}', \\
\hat{V}_{\text{ex}}\psi_0(\mathbf{r}) &= - \sum_{i=1}^N \psi_i(\mathbf{r}) \int \frac{\psi_i^*(\mathbf{r}')\psi_0(\mathbf{r}')}{|\mathbf{r} - \mathbf{r}'|} \langle \sigma_i | \sigma_0 \rangle d\mathbf{r}',
\end{aligned} \tag{54}$$

where N and N_{atm} denote the number of electrons and atoms, respectively; $\psi_i(\mathbf{r})$ and σ_i denote the molecular orbital and the spin state of the electron with index i , $\langle \sigma_i | \sigma_j \rangle = 1$ for electrons i and j with the same spin state, and $\langle \sigma_i | \sigma_j \rangle = 0$ otherwise; Z_A and \mathbf{R}_A are the nuclear charge and position of atom with index A .

Representing the rotated reference function in Eq. (48) with a linear combination of spherical harmonics using the Wigner- D matrix allows for efficient numerical evaluation of the structure factor using the coefficients calculated beforehand:

$$G_{\nu}(\theta, \chi) = e^{-\kappa\mu_F} \sum_{l=|m|}^{\infty} \sum_{m'=-l}^l I_{lm'}^{\nu} d_{mm'}^l(\theta) e^{-im'\chi}, \tag{55}$$

where the $e^{-im\phi}$ in the expansion of $D_{mm'}^l(\phi, \theta, \chi) = e^{-im\phi} d_{mm'}^l(\theta) e^{-im'\chi}$ is omitted because it doesn't play a part in the final result, and the coefficient $I_{lm'}^{\nu}$ has the following expression:

$$I_{lm'}^{\nu} = \int d\mathbf{r} \Omega_{lm'}^{\nu*}(\mathbf{r}) \hat{V}_{\text{c}}\psi_0(\mathbf{r}). \tag{56}$$

The original WFAT gives the instantaneous tunneling ionization rate $w = dW/dt$, however, without the dependence of k_{t} . In order to apply WFAT to prepare initial conditions of the electron samples, we have to reform the original WFAT to include k_{t} -dependent rate. Here we adopt the k_{t} -dependence in MO-ADK [Eq. (A8)], which gives

$$dW/dtd\mathbf{k}_{\text{t}} \propto k_{\text{t}}^{2|m|} e^{-\kappa k_{\text{t}}^2/F} \tag{57}$$

under the small- k_{t} limit. We modify the field factor $\mathcal{W}_{\nu}(F)$ according to the k_{t} -dependence above, which gives the modified field factor

$$\begin{aligned}
\mathcal{W}_{\nu}(F, k_{\text{t}}) &= \mathcal{W}_{\nu}(F) \frac{(\kappa/F)^{|m|+1}}{|m|!} k_{\text{t}}^{2|m|} e^{-\kappa k_{\text{t}}^2/F} \\
&\approx \frac{1}{2} \frac{\kappa^{|m|+2}}{F^{|m|+1} |m|!} \left(\frac{4\kappa^2}{F} \right)^{2n^* - 2n_{\xi} - |m| - 1} k_{\text{t}}^{2|m|} \exp \left[-\frac{2}{3} \frac{(k_{\text{t}}^2 + \kappa^2)^{3/2}}{F} \right],
\end{aligned} \tag{58}$$

where we choose the normalization coefficient so that

$$\mathcal{W}_{\nu}(F) = \int_0^{\infty} \mathcal{W}_{\nu}(F, k_{\text{t}}) 2\pi k_{\text{t}} dk_{\text{t}}. \tag{59}$$

In this way we obtain the k_{t} -dependent rate given by the WFAT:

$$\frac{dW^{\text{WFAT}}}{dt d\mathbf{k}_{\text{t}}} = \sum_{\nu} |G_{\nu}(\theta, \chi)|^2 \mathcal{W}_{\nu}[F(t), k_{\text{t}}]. \tag{60}$$

B. Trajectory Simulation and Quantum Phase

Given the initial conditions, the electrons released from the tunnel exit subsequently evolve classically in the combination of Coulomb and laser fields, following a classical trajectory, and the scheme is named the *Classical Trajectory Monte*

Carlo (CTMC). Apart from the position and momentum, a quantum phase could be endowed to the evolving trajectory, as in the *Quantum Trajectory Monte Carlo* (QTMC) and *Semiclassical Two-Step* (SCTS) Model, which largely retain quantum effects in the final PMD compared to the purely classical CTMC.

In this section we review the scheme of trajectory simulation and introduce the quantum phase methods available in `eTraj`.

1. Classical Trajectory Monte-Carlo (CTMC)

In the CTMC, each electron carries a probability W , following a classical trajectory, and finally ends up with a final momentum $\mathbf{p}_\infty = \mathbf{p}|_{t=\infty}$, which is our interested physical quantity.

The tunneled electrons, each having different tunneling times, initial positions and momenta, evolve under the Hamiltonian equation:

$$\dot{\mathbf{r}} = \nabla_{\mathbf{p}} H, \quad \dot{\mathbf{p}} = -\nabla_{\mathbf{r}} H, \quad (61)$$

and we use the Hamiltonian under the LG.

After the laser ends, the electron interacts only with the residual parent ion. At a distance from the parent ion, the electron interacts with the potential's Coulomb tail, and its Runge-Lenz vector

$$\mathbf{a} = \mathbf{p} \times \mathbf{L} - Z\mathbf{r}/r \quad (62)$$

can be viewed as asymptotically conserved. Taking advantage of the conservation of \mathbf{a} as well as the angular momentum and energy, we obtain the expression of the final momentum [83]:

$$\begin{aligned} \mathbf{p}_\infty &= p_\infty \frac{p_\infty(\mathbf{L} \times \mathbf{a}) - \mathbf{a}}{1 + p_\infty^2 L^2}, \\ p_\infty^2/2 &= p^2/2 - Z/r, \\ \mathbf{L} &= \mathbf{r} \times \mathbf{p}, \\ \mathbf{a} &= \mathbf{p} \times \mathbf{L} - Z\mathbf{r}/r, \end{aligned} \quad (63)$$

where \mathbf{r} and \mathbf{p} are quantities of the electron at any time after the laser ends. This scheme applies for electrons with positive energy, which are able to finally escape the parent ion and reach the detector. For electrons with negative energy, we assume that they get captured into Rydberg orbitals.

Finally, electrons with similar final momenta (i.e., in the same box of the final momentum grid) would be collected by summing up the probability they carry: $W_{\mathbf{p}} = \sum_i W_i$, and the final momentum spectrum is given by $W_{\mathbf{p}}$.

2. Quantum Trajectory Monte-Carlo (QTMC)

Compared with the CTMC, the QTMC scheme endows each electron trajectory with a quantum phase based on the Feynman path-integral approach [42], which is actually the S_{traj} in Eq. (19) with additional account of the Coulomb potential. The phase gets accumulated during the electron's excursion and is expressed as

$$\Phi^{\text{QTMC}} = S_{\text{traj}} = - \int_{t_r}^{\infty} \left[\frac{k^2}{2} + V(\mathbf{r}) + I_p \right] dt, \quad (64)$$

where t_r is the time when the electron exits the tunnel, and $\mathbf{k} = \dot{\mathbf{r}}$ denotes the momentum. Finally, the momentum spectrum is given by coherently summing up the probability amplitude leading to the same final momentum, and taking the square modulus of the summation result:

$$W_{\mathbf{p}} = \left| \sum_i \sqrt{W_i} e^{i\delta_i} \right|^2, \quad (65)$$

where \tilde{S}_i contains the initial phase of the prefactor and the phase accumulated during the tunneling process, as well as the trajectory motion:

$$\tilde{S} = \arg \mathcal{P}_p + \Re S_{\text{tun}} + S_{\text{traj}}. \quad (66)$$

The phase $\Re S_{\text{tun}}$ can be evaluated numerically, but can be simplified if we follow the non-adiabatic-expansion scheme in Sec. II A 2:

$$\begin{aligned} \Re S_{\text{tun}} &\approx \Re \int_{t_s}^{t_r} d\tau \left\{ \frac{1}{2} \left[\mathbf{p} + \mathbf{A}(t_r) - i t_i \mathbf{F}(t_r) + \frac{1}{2} t_i^2 \mathbf{F}'(t_r) \right]^2 + I_p \right\} \\ &= -[\mathbf{k}(t_r) \cdot \mathbf{F}(t_r)] \frac{t_i^2}{2} + o(t_i^2) \\ &\approx -\mathbf{k}_0 \cdot \mathbf{r}_0. \end{aligned} \quad (67)$$

The last line of Eq. (67), i.e., $-\mathbf{k}_0 \cdot \mathbf{r}_0$, vanishes for the SFA-SPANE and ADK initial condition methods due to vanishing longitudinal initial momentum ($k_{\parallel} = 0$).

It is also worthwhile noting that in the practical implementation, the upper limit of the integral in Eq. (64) does not have to be infinity. Since electrons arrive at the same final momentum share the same energy after the laser ends (at t_f), the integral

$$\int_{t_f}^{\infty} \left[\frac{k^2}{2} + V(\mathbf{r}) + I_p \right] dt \quad (68)$$

is same for electrons with the same final momentum. Therefore, in numerical implementation, the upper limit of the phase integral in Eq. (64) can be simply set as the end of the laser, i.e., the t_f , giving

$$S_{\text{traj}}^{\text{QTMC}} = - \int_{t_f}^{t_f} \left[\frac{k^2}{2} + V(\mathbf{r}) + I_p \right] dt. \quad (69)$$

3. Semiclassical Two-Steps (SCTS) Model

The SCTS model [45] improves the quantum phase in the QTMC scheme, giving

$$\Phi^{\text{SCTS}} = \Re S_{\text{tun}} + S_{\text{traj}} = \underbrace{-\mathbf{k}_0 \cdot \mathbf{r}_0}_{\Re S_{\text{tun}}} - \underbrace{\int_{t_0}^{\infty} \left[\frac{k^2}{2} + V(\mathbf{r}) - \mathbf{r} \cdot \nabla V(\mathbf{r}) + I_p \right] dt}_{S_{\text{traj}}}. \quad (70)$$

The difference between the SCTS phase [Φ^{SCTS} in Eq. (70)] and the QTMC phase [Φ^{QTMC} in Eq. (64)] lies in two aspects: The first is the initial phase $-\mathbf{k}_0 \cdot \mathbf{r}_0$ obtained in the tunneling process, which is non-zero for $k_{\parallel} \neq 0$ for non-adiabatic tunneling. The second is the $\mathbf{r} \cdot \nabla V(\mathbf{r})$ term in the integrand, which is omitted in the QTMC scheme. The difference arises from formulation schemes of the two methods, as the QTMC obtained the phase under the first-order perturbation theory, while the SCTS's formulation went beyond the perturbation theory. We note that we would only adopt the trajectory phase of the SCTS model, i.e., the S_{traj} in Eq. (70), because the tunneling phase $\Re S_{\text{tun}}$ is supposed to be included in the stage of initial condition preparation.

For the SCTS model, the phase integral in Eq. (70) in the interval $[t_f, \infty)$ cannot be simply neglected due to the presence of the $\mathbf{r} \cdot \nabla V(\mathbf{r})$ term. However, the integral of this term can be reduced to an analytical expression in case of Coulomb potential, called the post-pulse Coulomb phase:

$$S_{\text{traj},f}^{\text{C}}(t_f) = \int_{t_f}^{\infty} \mathbf{r} \cdot \nabla V(\mathbf{r}) dt = Z \int_{t_f}^{\infty} \frac{dt}{r} = -n^* \left[\ln g + \sinh^{-1} \left(\frac{\kappa}{g} \mathbf{r}_f \cdot \mathbf{p}_f \right) \right], \quad (71)$$

where $\mathbf{r}_f = \mathbf{r}(t_f)$, $\mathbf{p}_f = \mathbf{p}(t_f)$ and $g = \sqrt{1 + 2\kappa^2 L^2} = \sqrt{1 + 2\kappa^2 (\mathbf{r}_f \times \mathbf{p}_f)^2}$.

In this way we obtain the expression of the SCTS trajectory phase that is suitable for numerical implementation:

$$S_{\text{traj}}^{\text{SCTS}} = I_p t_r - \int_{t_r}^{t_f} \left[\frac{k^2}{2} + V(\mathbf{r}) - \mathbf{r} \cdot \nabla V(\mathbf{r}) \right] dt + S_{\text{traj},f}^{\text{C}}(t_f). \quad (72)$$

III. PROGRAM STRUCTURE AND MANUAL

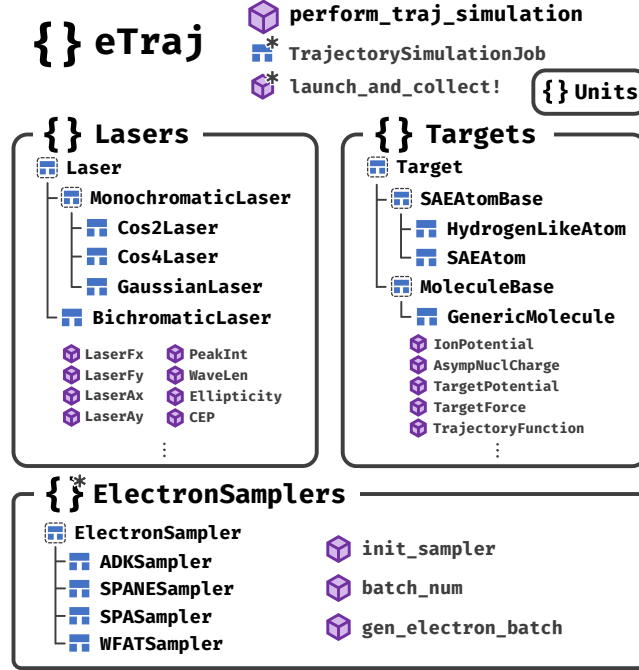


FIG. 1. Program structure diagram of eTraj.

The rough structure of eTraj is shown in Fig. 1. There are four key components in the program, namely Targets, Lasers, ElectronSamplers, and TrajectorySimulationJob. Each of these components plays a vital role within the library, forming an essential link in the chain of functionality.

A. Lasers Module

A typical monochromatic laser is composed of the carrier wave $\cos(\omega t + \phi)$ and the envelope function $f_{\text{env}}(t)$ (which is assumed to have a peak amplitude of 1). Given the amplitude of the vector potential A_0 , the time-dependent vector potential of the laser, which we assume to propagate in z direction and have x axis as the principle axis of polarization, reads

$$A(t) = A_0 f_{\text{env}}(t) [\cos(\omega t + \phi) \hat{x} + \varepsilon \sin(\omega t + \phi) \hat{y}], \quad (73)$$

with ω the laser angular frequency, ϕ the carrier-envelope phase (CEP) and ε the ellipticity.

In the Lasers module there are some available monochromatic laser objects implemented for use, namely Cos4Laser, Cos2Laser and GaussianLaser, which differ from each other in their envelope functions $f_{\text{env}}(t)$, and they are all subtypes of the MonochromaticLaser base type.

The Cos4Laser's vector potential has a \cos^4 -shaped envelope function:

$$f_{\text{env}}^{\cos^4} = \begin{cases} \cos^4 \left[\frac{\omega(t - t_0)}{2N} \right], & -NT/2 \leq t - t_0 \leq NT/2, \\ 0, & \text{otherwise,} \end{cases} \quad (74)$$

where N is the total cycle number, $T = 2\pi/\omega$ is the period and t_0 the peak time.

The `Cos2Laser` has a \cos^2 -shaped envelope function, similar to that of the `Cos4Laser`:

$$f_{\text{env}}^{\text{cos}^2} = \begin{cases} \cos^2 \left[\frac{\omega(t - t_0)}{2N} \right], & -NT/2 \leq t - t_0 \leq NT/2, \\ 0, & \text{otherwise.} \end{cases} \quad (75)$$

The `GaussianLaser` has a Gaussian-shaped envelope function, which is the most commonly used:

$$f_{\text{env}}^{\text{Gauss.}} = e^{-(t-t_0)^2/2\tau_\sigma^2} = e^{-\ln 2 \cdot (t-t_0)^2/\tau_{\text{FWHM}}^2}, \quad (76)$$

where τ_σ is the temporal width of the laser and $\tau_{\text{FWHM}} = 2\sqrt{\ln 2} \tau_\sigma$ denotes the laser's intensity profile's temporal FWHM (full-width at half maxima).

The signatures of the constructor methods of the monochromatic laser objects read below:

```
Cos4Laser(peak_int, wave_len|ang_freq, cyc_num|duration, ellip [,azi=0] [,cep=0] [,t_shift=0])
Cos2Laser(peak_int, wave_len|ang_freq, cyc_num|duration, ellip [,azi=0] [,cep=0] [,t_shift=0])
GaussianLaser(peak_int, wave_len|ang_freq, spread_cyc_num|spread_duration|FWHM_duration, ellip [,azi=0] [,cep=0]
↳ [,t_shift=0])
```

where a parameter inside square brackets indicates an optional choice, and the “|” character suggests a choice when providing the parameter. For a detailed description of the parameters, see Table I.

Parameter	Expression	Description	Unit
<code>peak_int</code>	$I_0 = A_0^2 \omega^2 (1 + \varepsilon^2)$	Peak intensity	W/cm ²
<code>wave_len</code>	$\lambda = c_0 T$	Wavelength	nm
<code>ang_freq</code>	ω	Angular frequency	a.u.
<code>ellip</code>	ε	Ellipticity ($-1 \leq \varepsilon \leq 1$, 0 indicates linear polarization and ± 1 indicates circular polarization)	—
<code>cyc_num</code>	N	[<code>Cos2Laser</code> and <code>Cos4Laser</code>] Number of total cycles	—
<code>duration</code>	NT	[<code>Cos2Laser</code> and <code>Cos4Laser</code>] Duration	a.u.
<code>spread_cyc_num</code>	$N_\sigma = \tau_\sigma / T$	[<code>GaussianLaser</code>] Temporal width converted to cycle numbers	—
<code>spread_duration</code>	τ_σ	[<code>GaussianLaser</code>] Temporal width	a.u.
<code>FWHM_duration</code>	τ_{FWHM}	[<code>GaussianLaser</code>] Temporal FWHM of the intensity profile	a.u.
<code>azi</code>	—	Azimuth angle of the polarization's principle axis relative to the x axis	rad
<code>cep</code>	ϕ	Carrier-Envelope-Phase	rad
<code>t_shift</code>	t_0	Time shift relative to the peak	a.u.

TABLE I. Input parameters of the constructor methods of the monochromatic laser objects in the `Lasers` module.

Apart from monochromatic lasers, the `BichromaticLaser` which combines two `MonochromaticLasers` is also implemented. A `BichromaticLaser` is initialized by the method:

```
BichromaticLaser(l1::MonochromaticLaser, l2::MonochromaticLaser [,delay=0])
```

with `delay` being the time delay of `l2` relative to `l1`.

Utilizing the `Unitful.jl` package which provides convenient unit conversion, it is possible to pass a `Unitful.Quantity` with other units, as the program would make conversions automatically. Some commonly-used units are exported in the submodule `eTraj.Units` and are within reach upon import, see note [84].

The example of usage is shown below, which runs in the Julia REPL (run-eval-print-loop) terminal [85]:


```

julia> using eTraj.Lasers

julia> l = Cos2Laser(peak_int=4e14, wave_len=800.0, cyc_num=2.0, ellip=0.0) # without units, following default units
[MonochromaticLaser] Envelope cos2, peak intensity 4.0e+14 W/cm2, wavelen=800 nm, 2 cycle(s), ε=0 [linearly polarized]

julia> using eTraj.Units # import the Units submodule to access units

julia> l = Cos4Laser(peak_int=0.4PW/cm2, ang_freq=1.5498eV, duration=26.7fs, ellip=1.0, cep=90°)
[MonochromaticLaser] Envelope cos4, peak intensity 4.0e+14 W/cm2, wavelen=800.00 nm, 10.01 cycle(s), ε=1 [circularly polarized], CEP=0.50 π

julia> l = GaussianLaser(peak_int=4e14W/cm2, wave_len=400nm, FWHM_duration=20fs, ellip=-1)
[MonochromaticLaser] Envelope Gaussian, peak intensity 4.0e+14 W/cm2, wavelen=400 nm, temporal width 9.00 cycle(s) [FWHM 20.00 fs], ε=-1
↳ [circularly polarized]

julia> l = BichromaticLaser(l1=Cos4Laser(peak_int=1.0PW/cm2, wave_len=800nm, cyc_num=10, ellip=1), l2=Cos4Laser(peak_int=1.0PW/cm2,
↳ wave_len=400nm, cyc_num=20, ellip=-1), delay=0.5fs)
[BichromaticLaser] delay Δt = 20.67 a.u. (0.50 fs)
├ [MonochromaticLaser] Envelope cos4, peak intensity 1.0e+15 W/cm2, wavelen=800 nm, 10 cycle(s), ε=1 [circularly polarized]
└ [MonochromaticLaser] Envelope cos4, peak intensity 1.0e+15 W/cm2, wavelen=400 nm, 20 cycle(s), ε=-1 [circularly polarized]

```

We note that the constructor methods should be invoked with keyword arguments, as is shown in the example.

B. Targets Module

The **Targets** module implements the abstraction of targets and provides parameters of some commonly-used targets.

The **HydrogenLikeAtom** and **SAEAtom** are both subtypes of the **SAEAtomBase** base type, which represents an atom under the SAE approximation. A key ingredient of atomic objects lies in the potential function of the residual ion after the electron gets ionized, which is the only difference between the two types.

The **HydrogenLikeAtom**'s potential function is of the form:

$$V(r) = -\frac{Z}{\sqrt{r^2 + a}}, \quad (77)$$

with a the soft-core parameter which avoids singularity of the potential during numerical simulation.

The **SAEAtom**'s potential function is adopted from Tong's model [86]:

$$V(r) = -\frac{Z + a_1 e^{-b_1 r} + a_2 r e^{-b_2 r} + a_3 e^{-b_3 r}}{\sqrt{r^2 + a}}, \quad (78)$$

where a_i and b_i are tunable parameters to fit the effective potential felt by the electron.

The signatures of the constructor methods of **HydrogenLikeAtom** and **SAEAtom** are listed below:

```

HydrogenLikeAtom(Ip, Z [,l=0] [,m=0] [,asymp_coeff=:hartree|<coeff>] [,quan_ax_theta=0] [,quan_ax_phi=0] [,soft_core=1e-10]
↳ [,name])
SAEAtom(Ip, Z [,l=0] [,m=0] [,asymp_coeff=:hartree|<coeff>] [,quan_ax_theta=0] [,quan_ax_phi=0] [,a1,b1,a2,b2,a3,b3]
↳ [,soft_core=1e-10] [,name])

```

A detailed description of the parameters is listed in Table II.

For the convenience of the user, there are some presets of commonly-used atoms, which can be accessed through the `get_atom` method. Available keys are accessed by invoking `get_available_atoms()`.

Finally, we present an example of using **HydrogenLikeAtom** and **SAEAtom** in REPL:

```

julia> using eTraj.Targets

julia> t = HydrogenLikeAtom(Ip=0.5, Z=1, name="H")
[HydrogenLikeAtom] Atom H, Ip=0.5000 (13.61 eV), Z=1

julia> using eTraj.Units

julia> t = SAEAtom(Ip=12.13eV, Z=1, l=1, a1=51.35554, b1=2.111554, a2=-99.92747, b2=3.737221, a3=1.644457, b3=0.4306465,
↳ asymp_coeff=1.3, name="Xe")
[SAEAtom] Atom Xe (p orbital, m=0), Ip=0.4458 (12.13 eV), Z=1

# example of get_atom

julia> t = get_atom("He1p")
[HydrogenLikeAtom] Atom He+, Ip=1.0000 (27.21 eV), Z=2

julia> t = get_atom("Xe"; m=1, quan_ax_theta=90°, quan_ax_phi=0°) # other parameters can be passed via keyword arguments
[SAEAtom] Atom Xe (p orbital, m=1), Ip=0.4458 (12.13 eV), Z=1, theta=(90.0°,0.0°)

```

Parameter	Description
Ip	Ionization potential (default unit is a.u.)
Z	Asymptotic charge of the residual ion
l	Angular quantum number
m	Magnetic quantum number
asymp_coeff	Asymptotic coefficient C_{xl} , setting :hartree indicates automatic calculation using Eq. (14)
quan_ax_theta	Quantization axis' polar angle in the LF
quan_ax_phi	Quantization axis' azimuth angle in the LF
name	Target's name
soft_core	Soft-core parameter
a1,b1,a2,b2,a3,b3	[SAEAtom] Tunable parameter to fit the effective potential

TABLE II. Input parameters of the constructor method of `HydrogenLikeAtom` and `SAEAtom` in the `Targets` module.

For molecule targets, the `GenericMolecule` type is implemented, whose structure is more complicated. A `GenericMolecule` stores information about the atoms that form the molecule, together with their coordinates, as well as the asymptotic coefficients [C_{lm} in Eq. (38)] and WFAT's integral coefficients [Eq. (56)], which are obtained using other quantum chemistry packages.

There are two ways to initialize a `GenericMolecule`: build from zero or from an existing file, see the definition below. The description of the corresponding parameters is listed in Table III.

```

GenericMolecule(atoms, atom_coords [,charge=0] [,spin=0] [,name] [,rot_alpha=0] [,rot_beta=0] [,rot_gamma=0])
LoadMolecule(ext_data_path; [,rot_alpha=0] [,rot_beta=0] [,rot_gamma=0])

```

As for the quantum chemistry calculation, we implemented the scheme in `PySCFMolecularCalculator` using the PySCF [87], which works on Linux and macOS platforms [Windows users can use the Windows Subsystem of Linux (WSL)]. The calculation scheme of the WFAT structure factor is adopted from `PyStructureFactor` [82]. Future extension is possible by implementing the supertype `MolecularCalculatorBase`. Since there are some presets of molecules

Parameter	Description
<code>atoms</code>	Atoms in the molecule, stored as a Vector of String
<code>atom_coords</code>	Atoms' coordinates in the molecule, stored as a N×3 matrix (default unit is Å)
<code>charge</code>	Total charge number (i.e., $Z - 1$)
<code>spin</code>	Total spin (each unpaired electron contributes 1/2)
<code>name</code>	Molecule's name
<code>rot_α,rot_β,rot_γ</code>	Euler angles ($z - y' - z''$ convention) specifying the molecule's orientation in LF (default unit is radian)
<code>ext_data_path</code>	[LoadMolecule] Path to the molecule's data which is stored externally

TABLE III. Input parameters of the initialization methods of `GenericMolecule` in the `Targets` module.

available via `get_mol`, we are not going to detail on the manual of running the calculation in the text.

The example of initializing and calculating the essential data of `GenericMolecule` in REPL is presented as follows:

```

julia> using eTraj.Targets, eTraj.Units

julia> mol = GenericMolecule(atoms=["O","C","O"], atom_coords=[0 0 -1.1600; 0 0 0; 0 0 1.1600]*Å, charge=0, name="Carbon
↳ Dioxide (CO₂)")
[GenericMolecule] Carbon Dioxide (CO₂)

julia> MolInitCalculator!(mol, basis="cc-pVTZ")
[ Info: [PySCFMolecularCalculator] Running molecular calculation ...

julia> MolCalcAsympCoeff!(mol, 0); MolCalcAsympCoeff!(mol, -1)
[ Info: [PySCFMolecularCalculator] Running calculation of asymptotic coefficients... (ionizing orbital HOMO)
[ Info: [PySCFMolecularCalculator] Running calculation of asymptotic coefficients... (ionizing orbital HOMO-1)

julia> MolCalcWFATData!(mol, 0); MolCalcWFATData!(mol, -1)
[ Info: [PySCFMolecularCalculator] Running calculation of WFAT structure factor data... (ionizing orbital HOMO)
[ Info: [PySCFMolecularCalculator] Running calculation of WFAT structure factor data... (ionizing orbital HOMO-1)

julia> MolSaveDataAs!(mol, "Molecule_CO2.jld2")
[ Info: [GenericMolecule] Data saved for molecule Carbon Dioxide (CO₂) at `Molecule_CO2.jld2`.

julia> mol_ = LoadMolecule("Molecule_CO2.jld2") # load from saved file
[GenericMolecule] Carbon Dioxide (CO₂)
Asymp coeff of HOMO-1 & HOMO available
WFAT data of HOMO-1 & HOMO available
#           E (Ha)  occp
:           :       :
13 LUMO+1  0.207  —
12 LUMO    0.175  —
11 HOMO   -0.542 -1|-
10 HOMO-1 -0.542 -1|-
9  HOMO-2 -0.714 -1|-
8  HOMO-3 -0.714 -1|-
:         :       :

```

C. Electron Sampling and Trajectory Simulation

The `ElectronSamplers` module provides means of generating initial electron samples using different initial condition methods. The `ElectronSampler` is an abstract supertype, with `ADKSampler`, `SPANESampler`, `SPASampler` and `WFATSampler` being its subtypes. When the user starts a trajectory simulation job by invoking `eTraj.perform_traj_simulation`, the method would further call the `init_sampler` method, which would assign the corresponding type of `ElectronSampler` in the background. These invocations execute in the background thus the `ElectronSamplers` module is kept internal (i.e., not exported for public invocation).

The `eTraj.perform_traj_simulation` method serves as a public entrance to performing a trajectory simulation. The method would automatically detect number of available threads (specified by passing command-line arguments “`-t <thread_num>`” when starting julia) and run the trajectory simulation in parallel. Table IV details on the input parameters of the method.

Here we brief on the working procedure of the method `eTraj.perform_traj_simulation`:

- First, the `eTraj.perform_traj_simulation` method initializes an `eTraj.TrajectorySimulationJob`, which stores the essential parameters. The electron sampler is assigned according to `init_cond_method`.
- Then, it repeatedly invokes the `eTraj.launch_and_collect!` method, where in each invocation a batch of electrons that get released at the same time t_r but have different transversal momenta \mathbf{k}_t is launched and collected using the corresponding simulation scheme.
 - The sampling behavior is controlled by the `sample_monte_carlo` parameter, if `sample_monte_carlo` is `true`, the time t_r of the electron batches and the momentum \mathbf{k}_t in each batch would be randomly sampled inside the given intervals specified by `sample_t_intv`, `mc_kd_max` and `mc_kz_max`; otherwise, the initial conditions of the electrons would be sampled in an equidistant manner, with the intervals controlled by `sample_t_intv`, `ss_kd_max` and `ss_kz_max`.
- After generating a batch of initial electrons, the `eTraj.launch_and_collect!` method simulates the electrons’ classical trajectories (potentially together with the phase), and then collects the electrons’ final momenta on the grid. Trajectory simulations are carried out using the `OrdinaryDiffEq.jl` package [88].
 - The grid’s size and spacing depends on the `final_p_max` and `final_p_num` parameters.
- Finally, the `eTraj.perform_traj_simulation` method generates the output file which contains the PMD and other necessary information in a Julia Data Format (JLD2) file or an HDF5 file.

The output file is a Julia JLD2 file, which is compatible with the HDF5 data format, and can be opened by the `JLD2.jl` package:

```
julia> using JLD2

julia> file = jldopen("ADK-CTMC_4e14_800nm_cos4_2cyc_CP.jld2")
JLDFile ... /ADK-CTMC_4e14_800nm_cos4_2cyc_CP.jld2 (read-only)
├─ info
├─ params_text          # parameters stored in YAML format
├─ params              # parameters stored in a Julia `Dict`
├─ px                 # coordinates of the `momentum_spec` on x-axis
├─ py                 # coordinates of the `momentum_spec` on y-axis
├─ momentum_spec      # PMD data stored in a Julia `Array`
├─ ion_prob            # total ionization probability
├─ ion_prob_uncollected # ionization probability of discarded electrons
└─ num_effective_traj  # total number of effective trajectories

julia> file["params_text"] ▷ print # equivalent to print(file["params_text"])
```

```
init_cond_method: ADK
laser:
  type: Cos4Laser
  peak_int: 4.0e14
  wave_len: 800.0
  :
target:
  type: HydrogenLikeAtom
  Ip: 0.5
  nucl_charge: 1
  :
sample_t_intv: (-100, 100)
sample_t_num: 20000
sample_monte_carlo: false
:
```

Parameter	Description	Default
<i>Required parameters</i>		
<code>init_cond_method</code>	Method used to determine the initial conditions of electrons. Candidates: <code>:ADK</code> , <code>:SPA</code> (SFA-SPA), <code>:SPANE</code> (SFA-SPANE) for targets of type <code>SAEAtomBase</code> or <code>MoleculeBase</code> ; <code>:WFAT</code> for <code>MoleculeBase</code> targets.	
<code>laser</code>	A <code>Lasers.Laser</code> object which stores parameters of the laser field.	
<code>target</code>	A <code>Targets.Target</code> object which stores parameters of the target.	
<code>dimension</code>	Dimensionality of the simulation (2 or 3). 2D simulation is carried out in the $x - y$ plane.	
<code>sample_t_intv</code>	Time interval for sampling initial electrons. Format: <code>(start, stop)</code> . Default unit: a.u.	
<code>sample_t_num</code>	Number of time samples.	
<code>traj_t_final</code>	Final time of each trajectory simulation. Default unit: a.u.	
<code>final_p_max</code>	Boundaries of final momentum grid. Grid ranges from <code>-pxMax</code> to <code>+pxMax</code> in the x direction, and the same for y and z directions. Format: <code>(pxMax, pyMax[, pzMax])</code>	
<code>final_p_num</code>	Numbers of final momentum grid points. If a value is 1, electrons will be collected regardless of the momentum on that dimension. Format: <code>(pxNum, pyNum[, pzNum])</code>	
<i>Required parameters for step sampling (SS) methods (sample_monte_carlo=false)</i>		
<code>ss_kd_max</code>	Boundary of k_{\perp} samples (in a.u.). k_{\perp} ranges from <code>-ss_kd_max</code> to <code>+ss_kd_max</code> .	
<code>ss_kd_num</code>	Number of k_{\perp} samples.	
<code>ss_kz_max</code>	[3D only] Boundary of k_z samples (in a.u.). k_z ranges from <code>-ss_kz_max</code> to <code>+ss_kz_max</code> .	
<code>ss_kz_num</code>	[3D only] Number of k_z samples.	
<i>Required parameters for Monte-Carlo (mc) sampling methods (sample_monte_carlo=true)</i>		
<code>mc_kt_num</code>	Number of k_t samples in a single time sample.	
<code>mc_kd_max</code>	Boundary of k_{\perp} (in a.u.). k_{\perp} ranges from <code>-mc_kd_max</code> to <code>+mc_kd_max</code> .	
<code>mc_kz_max</code>	[3D only] Boundary of k_z (in a.u.). k_z ranges from <code>-mc_kz_max</code> to <code>+mc_kz_max</code> .	
<i>Optional parameters</i>		
<code>traj_phase_method</code>	Method used to determine classical trajectories' phase. Candidates: <code>:CTMC</code> , <code>:QTMC</code> , and <code>:SCTS</code> . Note: The <code>WFAT</code> initial condition only supports <code>:CTMC</code> .	
<code>traj_rtol</code>	Relative error tolerance for solving classical trajectories.	<code>1e-6</code>
<code>output_fmt</code>	Output file format. Candidates: <code>:jld2</code> (JLD2) and <code>:h5</code> (HDF5).	<code>:jld2</code>
<code>output_compress</code>	Determines whether output files are compressed or not. Note: For JLD2 output format, compression requires explicit installation of the <code>CodecZlib.jl</code> package.	<code>:true</code>
<code>output_path</code>	Path to output file.	
<code>sample_cutoff_limit</code>	Probability cutoff limit for sampled electrons. Electrons with probabilities lower than the limit would be discarded.	<code>1e-16</code>
<code>sample_monte_carlo</code>	Determines whether Monte-Carlo sampling is used when generating electron samples.	<code>false</code>
<i>Optional parameters for atomic SFA-SPA, SFA-SPANE and ADK methods</i>		
<code>rate_prefix</code>	Prefix of the exponential term in the ionization rate. <code>:Exp</code> indicates no prefix; <code>:Pre</code> and <code>:PreCC</code> indicates inclusion of the prefactor \mathcal{P} with or without the Coulomb correction C^{CC} ; <code>:Jac</code> indicates inclusion of the Jacobian factor J which is related to the sampling method; <code>:Full</code> is equivalent to <code>Set([:PreCC, :Jac])</code> . To combine <code>:Pre</code> and <code>:Jac</code> , pass <code>Set([:Pre, :Jac])</code> .	<code>:Full</code>
<i>Optional parameters for target MoleculeBase</i>		
<code>mol_orbit_idx</code>	Index of selected orbital relative to the HOMO (e.g., <code>0</code> indicates HOMO, and <code>-1</code> indicates HOMO-1.) For open-shell molecules, according to α/β spins, should be passed in format <code>(spin, idx)</code> where for α orbitals <code>spin=1</code> and for β orbitals <code>spin=2</code> .	<code>0</code>
<i>Optional parameters for interface</i>		
<code>show_progress</code>	Whether to display progress bar.	<code>true</code>

TABLE IV. Input parameters of the `eTraj.perform_traj_simulation` method.

IV. ILLUSTRATIVE EXAMPLES

In this section, we provide a selection of examples that demonstrate the typical use cases of `eTraj`, showcasing its capabilities in addressing the most common scenarios. The example and the corresponding post-processing codes are provided in the `examples/` directory.

Each script file with a filename like “`test_*.jl`” performs a set of trajectory simulations using `eTraj` and generates the output JLD2 file in the working directory, and each script whose filename matches “`plot_*.jl`” reads the corresponding JLD2 file and generates a figure.

A. Attoclock Experiment and the Influence of Initial Condition Methods

This example is adapted from Ref. [67].

In the present example of the attoclock experiment, an ultra-short pulse of circular polarization is employed to explore the ultrafast attosecond dynamics such as the tunneling time delay. In this example we would perform simulation of an attoclock experiment using different initial condition methods, namely ADK, SFA-SPANE and SFA-SPA, which reveals the influence of non-adiabatic effects to the attoclock signal. We choose CTMC as the phase method because the quantum interference effect is not significant in this example. In our theoretical framework, the simulation schemes are named after “ADK-CTMC”, “SFA-SPANE-CTMC” and “SFA-SPA-CTMC”, respectively.

```

examples/test_2cycs_CP.jl
1 using eTraj
2 using eTraj.Targets, eTraj.Lasers, eTraj.Units
3
4 l = Cos4Laser(peak_int=0.4PW/cm^2, wave_len=800.0nm, cyc_num=2, ellip=1.0)
5 t = get_atom("H")
6
7 for init_cond in [:ADK, :SPANE, :SPA]
8     perform_traj_simulation(
9         init_cond_method = init_cond,
10        laser            = l,
11        target           = t,
12        dimension        = 2,           # 2D simulation, x-y plane only
13        sample_t_intv     = (-100,100), # equivalent to `(-2.42fs, 2.42fs)`
14        sample_t_num      = 20000,     # will sample 20000 equidistant time points between -100 and 100 a.u.
15        traj_t_final      = 120,       # the traj end at 120 a.u., equivalent to `2.90fs`
16        final_p_max       = (2.5,2.5), # the momentum spec collection grid's border (-2.5 to +2.5 a.u.)
17        final_p_num       = (500,500), # the momentum spec collection grid's size (500x500)
18        ss_kd_max         = 2.0,
19        ss_kd_num         = 10000,     # will sample 10000 equidistant k⊥ points between -2 to +2 a.u.
20        output_path       = "$(init_cond)-CTMC_4e14_800nm_cos4_2cyc_CP.jld2",
21        traj_phase_method = :CTMC
22    )
23 end

```

The momentum spectra are shown in Fig. 2. Due to the exponential dependence of ionization rate on the field strength, the PMD exhibits a crescent shape near the peak of the negative vector potential $-A(t)$. In an adiabatic tunneling scenario, which corresponds to the ADK initial condition, the trace of $-A(t)$ is expected to match the median of the crescent shape. While for non-adiabatic tunneling, the distribution of the initial transverse momentum k_t at the tunnel exit centers at a nonzero value, which results in expansion of the crescent shape and the enhancement of overall ionization probability, as can be seen in the figure. Moreover, the PMD obtained with the SFA-SPANE and SFA-SPA initial conditions shows similar shape and total ionization probability, which demonstrate the SFA-SPANE’s advantage of preserving the non-adiabatic effects with much less computational cost than the SFA-SPA.

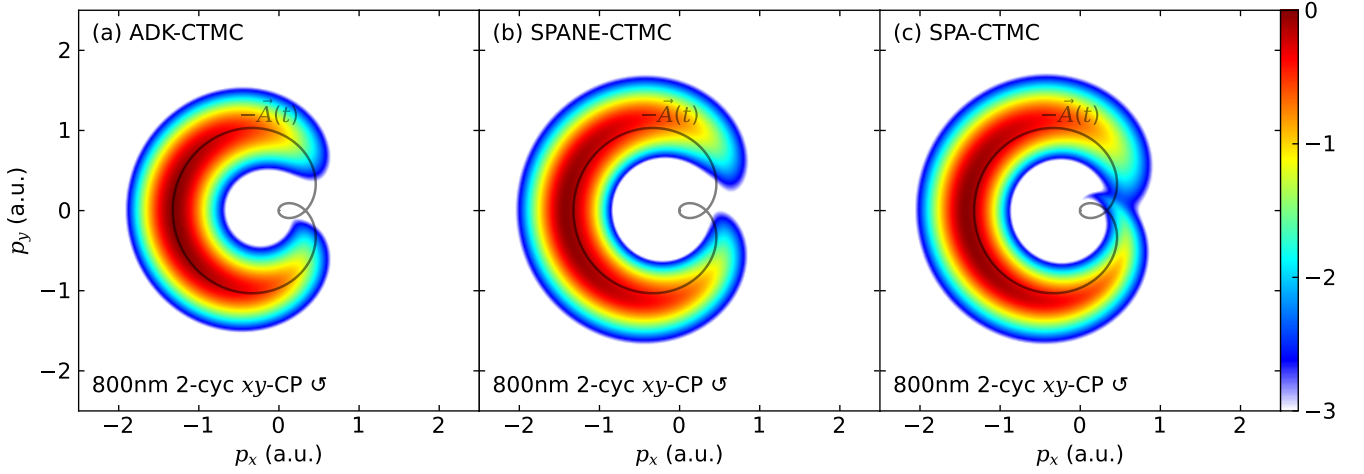


FIG. 2. Signals of an attoclock experiment obtained from CTMC simulation with the ADK (left), the SFA-SPANE (middle), and the SFA-SPA (right) initial conditions (logarithmic scale, each normalized to the maximum value). The laser is a 2-cycle circularly-polarized 800-nm pulse with a \cos^4 shape and peak intensity of 0.4 PW/cm^2 , which polarizes in the $x - y$ plane. The target is a hydrogen atom initially at the ground state. Trace of $-\vec{A}(t)$ is shown as a gray line in each sub-figure.

B. Interaction with Linearly-polarized Pulses and the Influence of Quantum Phase

This example is adapted from Ref. [45], which introduced the initial SCTS model.

When an atom is exposed to an intense linearly-polarized pulse, the atom might absorb photons more than it requires for the electron to ionize, leading to outer ring-like structures in the PMD, which we refer to as the well-known above-threshold ionization (ATI). The ATI is originally interpreted as excessive absorption of photons in the “multi-photon absorption” picture, while in the tunneling scenario, the ATI structures also have interpretable physical meanings: the intercycle interference of electron wave packets which tunneled through the potential barrier at each peak of the laser field. This allows for reproduction of the ATI structures using the semiclassical trajectory-based methods.

Apart from the ATI rings, the low-energy features of the PMD are also of broad interest, which usually exhibit a fan-like structure. This structure is contributed mainly by electrons with an angular momentum close to a specific value L_0 and are hence predictable theoretically [89, 90].

The following two pieces of code performs a trajectory simulation which employs an 8-cycle and an ultra-short single-cycle linearly-polarized near-infrared (NIR) pulse, with the PMD shown in Figs. 3 and 4. To be faithful to the original work (Ref. [45]) where the ADK initial condition was used with no prefactor included ($\mathcal{P} = 1$), we used the ADK-QTMC and ADK-SCTS schemes and set `rate_prefix=:Exp`. Comparison between the PMD obtained with the QTMC and SCTS phase methods reveals underestimation of the Coulomb interaction’s influence on the phase by the QTMC method, which is observed in the number of nodal lines in the low-energy structures.

```

examples/test_8cyccs_LP.jl
1 using eTraj
2 using eTraj.Targets, eTraj.Lasers, eTraj.Units
3
4 l = Cos2Laser(peak_int=90.0TW/cm^2, wave_len=800.0nm, cyc_num=8, ellip=0.0)
5 t = get_atom("H")
6
7 for phase_method in [:QTMC, :SCTS]
8     perform_traj_simulation(
9         init_cond_method = :ADK,
10        laser              = l,
11        target             = t,
12        dimension          = 2,

```

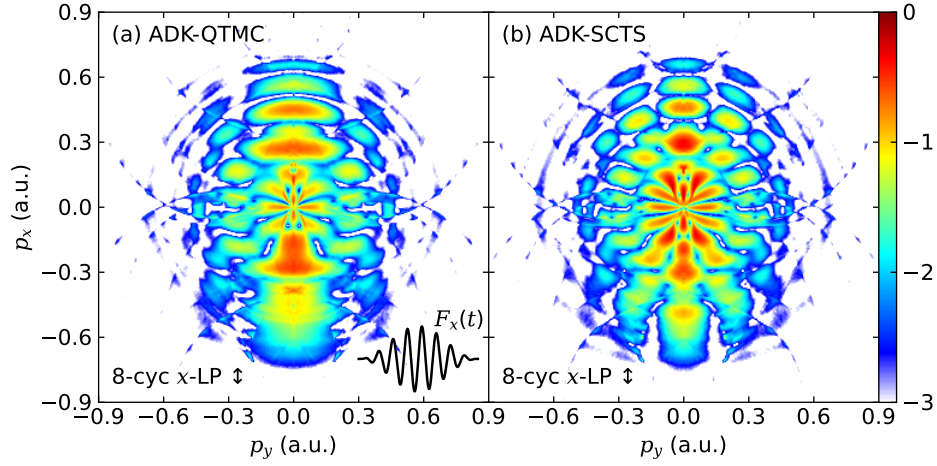



FIG. 3. Low-energy structure of the PMD from interaction of a hydrogen atom with an 8-cycle linearly-polarized laser pulse obtained using QTMC (left) and SCTS (right) phase methods (logarithmic scale, each normalized to the maximum value). The laser polarizes along the x axis and its wavelength is 800 nm, with its peak intensity being 90 TW/cm^2 . The shape of the field strength is shown in the left sub-figure.

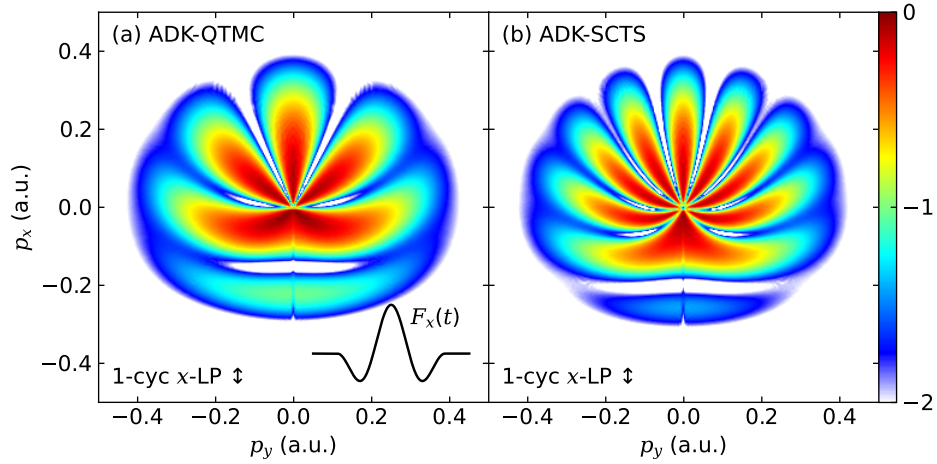


FIG. 4. Low-energy structure of the PMD from the interaction of a hydrogen atom with a single-cycle linearly-polarized laser pulse obtained using QTMC (left) and SCTS (right) phase methods (logarithmic scale, each normalized to the maximum value). The laser is an 800-nm single-cycle pulse which polarizes along the x axis, and the peak intensity is 90 TW/cm^2 . The CEP of the laser is set to $\pi/2$ in order for such a shape to be shown due to sensitivity of the PMD to the CEP for ultra-short pulses. The shape of the field strength is shown in the left sub-figure.

```

13     sample_t_intv      = (-350,350),
14     sample_t_num      = 50000,
15     traj_t_final      = 500,
16     final_p_max       = (1.0,1.0),
17     final_p_num       = (500,500),
18     ss_kd_max         = 1.0,
19     ss_kd_num         = 20000,
20     output_path       = "ADK-$(phase_method)_9e13_800nm_8cyc_LP_ExpRate.jld2",
21     traj_phase_method = phase_method,
22     rate_prefix       = :Exp
23 )

```

```
24 end
```

```
examples/test_1cyc_LP.jl
```

```
1 using eTraj
2 using eTraj.Targets, eTraj.Lasers, eTraj.Units
3
4 l = Cos2Laser(peak_int=90.0TW/cm^2, wave_len=800.0nm, cyc_num=1, cep=π/2, ellip=0.0)
5 t = get_atom("H"; soft_core=1e-12)
6
7 for phase_method in [:QTMC, :SCTS]
8     perform_traj_simulation(
9         init_cond_method = :ADK,
10        laser             = l,
11        target            = t,
12        dimension         = 2,
13        sample_t_intv     = (-50,50),
14        sample_t_num      = 30000,
15        traj_t_final      = 100,
16        final_p_max       = (1.0,1.0),
17        final_p_num       = (500,500),
18        ss_kd_max         = 1.5,
19        ss_kd_num         = 10000,
20        output_path       = "ADK-$(phase_method)_9e13_800nm_1cyc_LP_ExpRate.jld2",
21        traj_phase_method = phase_method,
22        rate_prefix       = :Exp
23    )
24 end
```

C. Interaction with an $\omega - 2\omega$ Bichromatic Clover-shaped Laser

A bichromatic laser which consists of a fundamental and its second harmonic frequency component, is widely used to construct a variety of specific tailored waveforms for manipulation and exploration of the ultrafast dynamics of light-matter interactions [91–95].

In this example, we use a bichromatic laser pulse which combines two counter-rotating circularly-polarized laser pulses of 800 nm and 400 nm wavelengths. By adjusting the relative intensity of the two frequency components, the waveform of the pulse can be tailored to exhibit a clover-like shape (see Fig. 5), which facilitates control of the emission direction of the ejected electrons. The PMD for different laser intensities is shown in Fig. 6.

```
examples/test_Bichromatic_CCP.jl
```

```
1 using eTraj
2 using eTraj.Targets, eTraj.Lasers, eTraj.Units
3
4 for int in [1e14, 3e14, 5e14, 7e14]
5     @info "Running I0=$(int) W/cm^2"
6     l1 = Cos2Laser(peak_int=int*W/cm^2, wave_len=800.0nm, cyc_num=8, ellip= 1.0)
7     l2 = Cos2Laser(peak_int=int*W/cm^2, wave_len=400.0nm, cyc_num=16, ellip=-1.0)
8     l = BichromaticLaser(l1=l1, l2=l2)
9     t = get_atom("H")
10    perform_traj_simulation(
11        init_cond_method = :ADK,
12        laser             = l,
13        target            = t,
```

```

14     dimension           = 2,
15     sample_t_intv      = (-350,350),
16     sample_t_num       = 10000,
17     traj_t_final       = 450,
18     final_p_max        = (2.5,2.5),
19     final_p_num        = (500,500),
20     ss_kd_max          = 1.0,
21     ss_kd_num          = 5000,
22     output_path        = "ADK-SCTS_Bichromatic_$(int)_800+400nm_8+16cyCs_CounterCP.jld2",
23     traj_phase_method  = :SCTS,
24     rate_prefix        = Set([:Pre,:Jac])
25 )
26 end

```

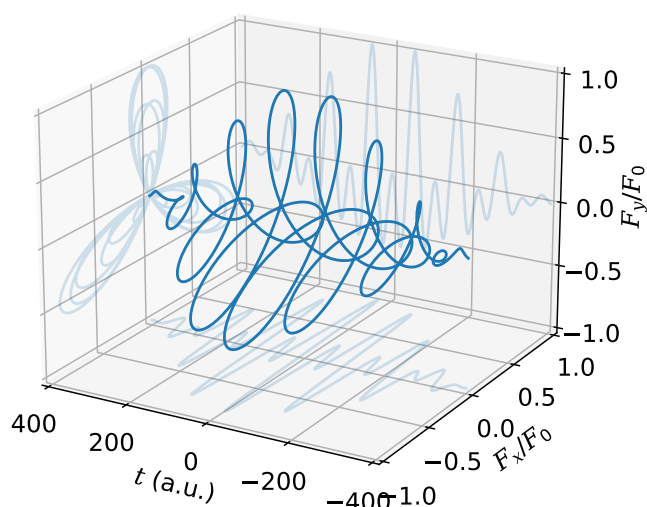


FIG. 5. Waveform of the electric field of an $\omega - 2\omega$ bichromatic counter-rotating circularly-polarized laser pulse. The fundamental (800 nm) and the second harmonic (400 nm) components of the laser share the same peak intensity and duration (8 cycles of the fundamental pulse).

D. WFAT-CTMC Simulation of Molecular Targets

The WFAT provides a precise means of calculating the probability of tunneling ionization of molecules, especially for complex molecular targets. In this section we present an example of using the WFAT-CTMC simulation scheme for molecular targets.

```

examples/test_Molecules.jl
1 using eTraj
2 using eTraj.Targets, eTraj.Lasers, eTraj.Units
3
4 l = Cos2Laser(peak_int=4e14W/cm^2, wave_len=800.0nm, cyc_num=6, ellip=1.0)
5 t = [get_mol("Hydrogen"; rot_β=90°),
6     get_mol("Carbon Monoxide"; rot_β=90°),

```

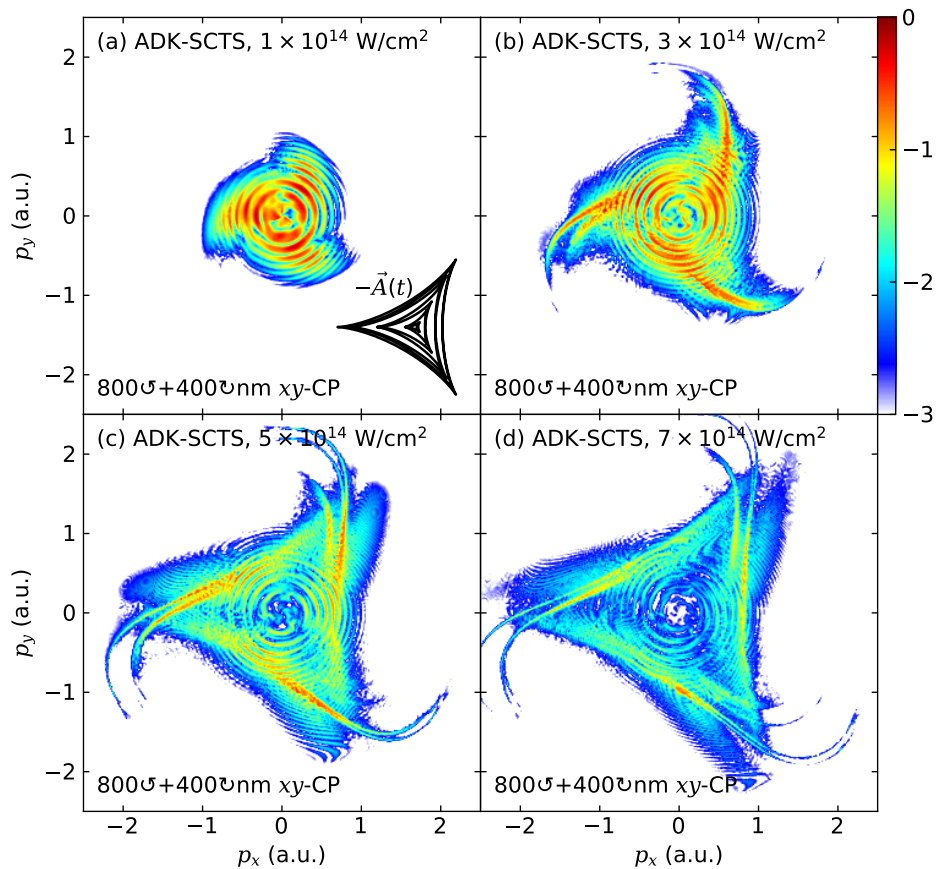


FIG. 6. PMDs of the interaction of a hydrogen atom with an $\omega - 2\omega$ bichromatic counter-rotating circularly-polarized laser pulse of different peak intensities (logarithmic scale, each normalized to the maximum value). The laser pulse's waveform of electric field and parameters are shown in Fig. 5, and the trace of $-\vec{A}(t)$ is shown in the first sub-figure.

```

7   get_mol("Oxygen"; rot_beta=90°),
8   get_mol("Oxygen"; rot_beta=90°),
9   get_mol("Benzene"; rot_beta=90°),
10  get_mol("Benzene"; rot_beta=90°)]
11  orbit_ridx = [0, 0, (1,0), (1,-1), 0, -1]
12  path = [
13      "WFAT-CTMC_Hydrogen_HOMO_4e14_800nm_6cyc_CP.jld2",
14      "WFAT-CTMC_CarbonMonoxide_HOMO_4e14_800nm_6cyc_CP.jld2",
15      "WFAT-CTMC_Oxygen_alpha-HOMO_4e14_800nm_6cyc_CP.jld2",
16      "WFAT-CTMC_Oxygen_alpha-HOMO-1_4e14_800nm_6cyc_CP.jld2",
17      "WFAT-CTMC_Benzene_HOMO_4e14_800nm_6cyc_CP.jld2",
18      "WFAT-CTMC_Benzene_HOMO-1_4e14_800nm_6cyc_CP.jld2"
19  ]
20  for i in eachindex(t)
21      perform_traj_simulation(
22          init_cond_method = :WFAT,
23          laser             = l,
24          target            = t[i],
25          dimension         = 2,
26          sample_t_intv    = (-300,300),
27          sample_t_num     = 10000,
28          traj_t_final     = 350,

```

```

29     final_p_max      = (2.0,2.0),
30     final_p_num      = (500,500),
31     ss_kd_max        = 2.0,
32     ss_kd_num        = 5000,
33     output_path      = path[i],
34     traj_phase_method = :CTMC, # WFAT supports CTMC only
35     mol_orbit_idx    = orbit_idx[i]
36 )
37 end

```

In this code, we set the molecules' orientation such that the z -axis in the MF is parallel to the x -axis in the LF, which can be realized by setting $\text{rot}_\beta=90^\circ$ (equivalent to a 90° counterclockwise rotation of the molecule around the y -axis). The laser is a circularly polarized 800-nm laser pulse, whose duration is set to 6 cycles to ensure the symmetry of the PMD for an isotropic atom, which facilitates the imaging of the molecules' orbitals through the PMD: a node or a dark curve would show up in the PMD if the laser's electric field vector crosses or scans inside a nodal plane of the orbital's wavefunction.

The PMDs obtained from different molecule's HOMO orbitals are shown in Fig. 7. The structures of the PMDs reflect the geometries of the orbitals, which are also mirrored in the orientation-dependent structure factors, as shown in Fig. 8.

Fig. 7 (a) shows the PMD of the hydrogen molecule's HOMO orbital $1\sigma_g$, which is mainly contributed by the in-phase combination of two $1s$ orbitals from the two hydrogen atoms. The overall shape of the orbital is similar to a sphere, which is consistent with the lowest order [$\nu = (n_\xi, m) = (0, 0)$] squared structure factor $|G_{00}|^2$ shown in Fig. 8 (a), and finally leads to the evenly-distributed ring-like shape of the PMD.

The carbon monoxide (CO) molecule is a heteronuclear diatomic molecule, whose HOMO orbital is named after $3\sigma_g$. The $3\sigma_g$ orbital of CO molecule is different from a conventional σ_g orbital of a homonuclear molecule in that the electron density is concentrated more on the carbon atom [see Fig. 8 (b)], which results in a dramatic increase in the squared structure factor and ionization probability when the negative electric field points towards the carbon atom. Such a localized peak in the ring structure is observed in the PMD of CO molecule in Fig. 7 (b).

The HOMOs of the oxygen (O_2) and benzene (C_6H_6) molecules (in MF) are shown in Figs. 8 (c) and (d), which are degenerate orbitals of π symmetry. The oxygen's ' α -HOMO' (one of $2p\pi_u$) and the benzene's ' α -HOMO' ($2p\pi_3$), after the given rotation ($\text{rot}_\beta=90^\circ$), have $x-z$ and $y-z$ as their nodal planes, hence the rotating electric field in the $x-y$ plane 'sees' a four-lobe structure, which is revealed in the PMDs in Figs. 7 (c1) and (d1). Whereas the oxygen's ' α -HOMO-1' (another one of $2p\pi_u$) and the benzene's ' α -HOMO-1' ($2p\pi_2$), each have a nodal plane on the $x-y$ plane, which indicates that in the zeroth order ($m = 0$), the outgoing electron waves that are contributed by the '+' parts and the '-' parts of the orbital cancel out each other, leading to a net-zero ionization probability. For non-zero- m channels we have $\mathcal{W}_\nu(F, k_t = 0) \equiv 0$ [see Eq. (58)], hence a nodal ring which corresponds to zero initial momenta $k_t = 0$ would appear in the PMDs of Figs. 7 (c2) and (d2). Under such circumstance, the ionization gets suppressed, and the first-order channels ($m = \pm 1$) would take dominance in the contribution of ionization probability.

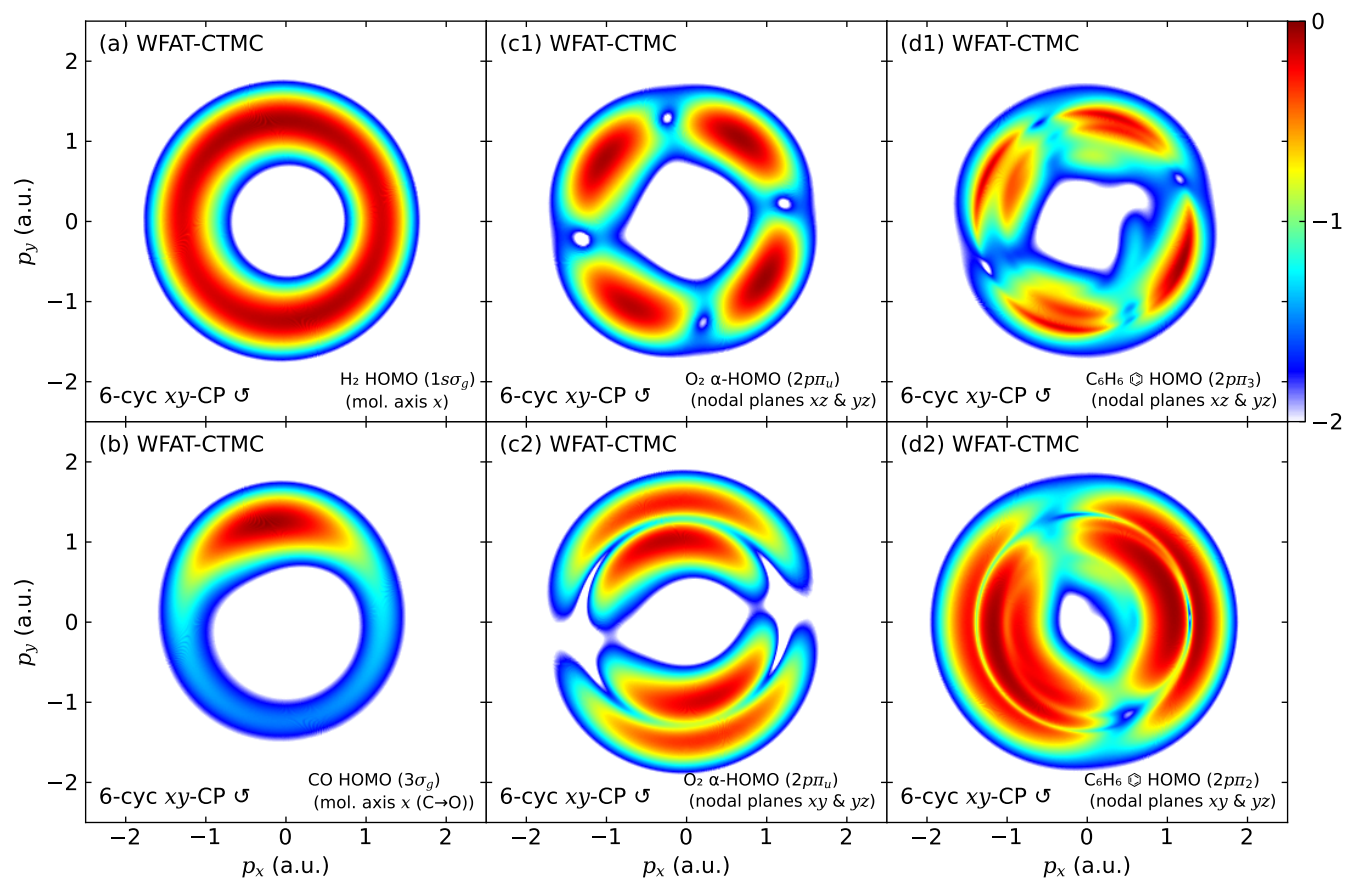


FIG. 7. PMDs of the interaction of different molecules' HOMOs with a 6-cycle circularly-polarized laser pulse obtained by the WFAT-CTMC scheme (logarithmic scale, each normalized to the maximum value). The laser's peak intensity is 0.4 PW/cm^2 and the wavelength is 800 nm.

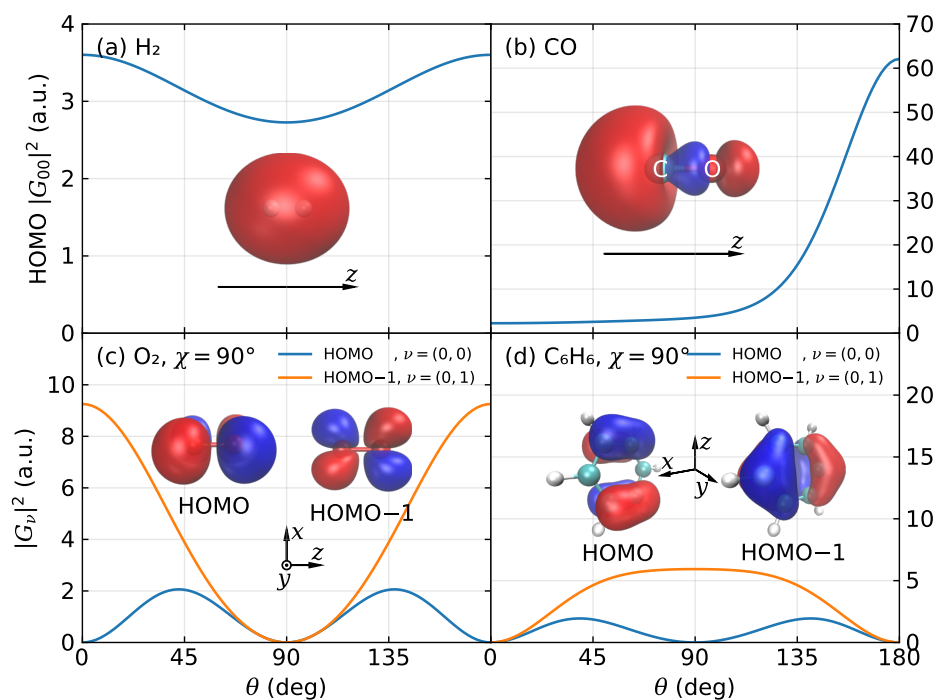


FIG. 8. Squared structure factors $|G_{\nu}(\theta, \chi = 90^\circ)|^2$ and the wavefunction isosurface diagram of the different molecules' HOMOs (in MF). The 'HOMO' and 'HOMO-1' orbitals are actually degenerate and are only used to distinguish between each other in the program. Wavefunction diagrams are created using the VMD [96].

V. CONCLUSIONS AND PROSPECTS

The classical/semiclassical trajectory-based methods are one of the most widely used methods for simulating and studying strong-field phenomena. In this article, we have presented a unified theoretical framework for these methods as well as the **eTraj** program package which performs trajectory simulations to determine the photoelectron momentum distribution of atoms and molecules in strong-field ionization processes. The **eTraj** provides an out-of-the-box solution for studying such phenomena, which also features versatility and user-friendliness. Besides the current functionalities, we are also planning for future extensions to **eTraj**, which include trajectory simulation beyond the dipole approximation and tracking of selected electron trajectories. We expect **eTraj** to become an indispensable tool for the strong-field physics community, enabling researchers to push the boundaries of the understanding of light-matter interactions with ease.

Appendix A: Ionization Rate of SFA-SPA in the Adiabatic Limit and the Coulomb-correction Term

Under the adiabatic limit, transition amplitude of SFA-SPA, i.e., Eq. (33), can be expanded to obtain a more concrete expression.

Let's start from the spherical harmonics $Y_{lm}[\hat{\mathbf{k}}(t_s)]$ in Eq. (34), the spherical harmonics is expressed as

$$Y_{lm}(\theta, \phi) = (-1)^m \sqrt{\frac{2l+1}{2} \frac{(l-m)!}{(l+m)!}} P_l^m(\cos \theta) \frac{e^{im\phi}}{\sqrt{2\pi}}, \quad (\text{A1})$$

with P_l^m the associated Legendre polynomial, and the z quantization axis is along the field polarization direction. Although $\hat{\mathbf{k}}(t_s)$ is a complex vector, the term $\cos \theta$ follows the conventional definition, according to Eq. (30) in Ref. [63]:

$$\cos \theta = \frac{\mathbf{k}(t_s) \cdot \mathbf{F}(t_r)}{\sqrt{\mathbf{k}(t_s) \cdot \mathbf{k}(t_s)} F(t_r)} = \sqrt{1 + \frac{k_t^2}{\kappa^2}}. \quad (\text{A2})$$

Substituting Eq. (A2) into Eq. (A1), utilizing the connection formula of $P_l^m(x)$ (Eq. (14.9.3) of Ref. [97]):

$$P_l^{-m}(x) = (-1)^m \frac{(l-m)!}{(l+m)!} P_l^m(x), \quad (\text{A3})$$

as well as the asymptotic behavior of $P_l^m(x)$ for $x \rightarrow 1^+$ (Eqs. (14.8.7) and (14.8.8) of Ref. [97]):

$$P_l^m(x) \sim \frac{1}{|m|!} \left(\frac{x-1}{2}\right)^{|m|/2} \times \begin{cases} (l+m)!/(l-m)!, & \text{for } m = 0, 1, 2, \dots, \\ 1, & \text{for } m = -1, -2, \dots, \end{cases} \quad (\text{A4})$$

we obtain the leading-order term of $Y_{lm}[\hat{\mathbf{k}}(t_s)]$ for small k_t :

$$Y_{lm}[\hat{\mathbf{k}}(t_s)] \sim Q_{lm} \frac{(k_t/\kappa)^{|m|} e^{im\phi}}{2^{|m|} |m|! \sqrt{2\pi}}, \quad (\text{A5})$$

where the coefficient

$$Q_{lm} = (-1)^m \sqrt{\frac{2l+1}{2} \frac{(l+|m|)!}{(l-|m|)!}}. \quad (\text{A6})$$

The next issue is concerned with the Jacobian factor $J(t_r, k_\perp)$ [Eq. (25)]. Under the adiabatic limit, the Jacobian is evaluated to a simple result:

$$J(t_r, k_\perp) = \left| \frac{\partial(p_x, p_y)}{\partial(t_r, k_\perp)} \right| = F(t_r) + \frac{k_\perp}{F^2(t_r)} [F_x(t_r)F_y'(t_r) - F_x'(t_r)F_y(t_r)] = F(t_r), \quad (\text{A7})$$

where the second equality is valid under $k_\parallel = 0$, while the third is valid further under the adiabatic condition $F'(t_r) = 0$, and we have $p_x = k_\perp F_y(t_r)/F(t_r) - A_x(t_r)$ and $p_y = -k_\perp F_x(t_r)/F(t_r) - A_y(t_r)$.

Combining the results above we have

$$\begin{aligned} \frac{dW}{dt_r d\mathbf{k}_t} &\approx J(t_r, k_\perp) |\mathcal{P}_p^{\text{ADK}}(t_s)|^2 \exp\left[-\frac{2}{3} \frac{(k_t^2 + \kappa^2)^{3/2}}{F}\right] \\ &= \frac{C_{\kappa l}^2}{\pi} \left[\frac{\Gamma(n^*/2 + 1)}{|m|!} \right]^2 |Q_{lm}|^2 2^{2n^* - 2|m| + 1} F^{-n^*} \kappa^{4n^* - 2|m| + 1} k_t^{2|m|} (\kappa^2 + k_t^2)^{-(n^* + 1)/2} \exp\left[-\frac{2}{3} \frac{(k_t^2 + \kappa^2)^{3/2}}{F}\right]. \end{aligned} \quad (\text{A8})$$

Integrate Eq. (A8) by \mathbf{k}_t in the polar coordinate under the approximation of small k_t :

$$\begin{aligned} &\int d\mathbf{k}_t k_t^{2|m|} (\kappa^2 + k_t^2)^{-(n^* + 1)/2} \exp\left[-\frac{2}{3} \frac{(k_t^2 + \kappa^2)^{3/2}}{F}\right] \\ &\approx 2\pi \kappa^{-(n^* + 1)} \exp\left(-\frac{2\kappa^3}{3F}\right) \int_0^\infty dk_t k_t^{2|m| + 1} \exp\left(-\frac{\kappa k_t^2}{F}\right) \\ &= \pi F^{|m| + 1} \kappa^{-n^* - |m| - 2} |m|! \exp\left(-\frac{2\kappa^3}{3F}\right), \end{aligned} \quad (\text{A9})$$

and we arrive at

$$w = \frac{dW}{dt_r} = C_{\kappa l}^2 \left[\Gamma \left(\frac{n^*}{2} + 1 \right) \right]^2 \frac{|Q_{lm}|^2}{|m|!} 2^{n^* - 2|m| + 1} F^{-n^* + |m| + 1} \kappa^{3n^* - 3|m| - 1} \exp \left(-\frac{2\kappa^3}{3F} \right). \quad (\text{A10})$$

Eq. (A10) is similar to the ADK ionization rate [98, 99], but they differ in the power coefficients of factors 2, F and κ . The discrepancy between the two expressions arises from the overlook of the influence of the Coulomb potential to the phase S_p in our derivation, while in our theoretical formulation, we only include this effect partially by using the asymptotic wavefunction in the Coulomb potential, in Eq. (12). In Refs. [100–102], another approach which utilized the trajectory-based perturbation method to study the influence of Coulomb interaction was performed, which gives the Coulomb-correction (CC) term:

$$\delta S_p(t_s) = -in^* \ln \frac{2\kappa^3}{F(t_r)}, \quad (\text{A11})$$

which resulted in the correction to the ionization rate of the *short range* (SR) case:

$$w^{\text{Coulomb}} = \exp(-2\Im \delta S_p) w^{\text{SR}} = \left(\frac{2\kappa^3}{F} \right)^{2n^*} w^{\text{SR}}. \quad (\text{A12})$$

To apply the Coulomb-correction term to Eq. (A10), we have to first remove our partial Coulomb correction by setting $n^* = 0$, which gives the short range ionization rate w^{SR} . After applying the correction in Eq. (A12), we retrieve the expression of the ionization rate which coincides with the ADK rate:

$$w^{\text{ADK}} = \frac{C_{\kappa l}^2 |Q_{lm}|^2}{|m|!} 2^{n^* - 2|m| + 1} F^{-2n^* + |m| + 1} \kappa^{6n^* - 3|m| - 1} \exp \left(-\frac{2\kappa^3}{3F} \right). \quad (\text{A13})$$

It implies that an additional Coulomb-correction factor to our ionization probability in Sec. II A based on SFA might be helpful in better alignment with the experimental results:

$$C^{\text{CC,ADK}} = \left(\frac{2\kappa^3}{F} \right)^{n^*} \left[\Gamma \left(\frac{n^*}{2} + 1 \right) \right]^{-2}. \quad (\text{A14})$$

Ref. [102] gives the correction term that is applicable for arbitrary Keldysh parameter:

$$C^{\text{CC}} = \left(\frac{2\kappa^3}{F} \right)^{n^*} (1 + 2\gamma/e)^{-n^*} \left[\Gamma \left(\frac{n^*}{2} + 1 \right) \right]^{-2}, \quad (\text{A15})$$

which we have adopted in `eTraj`.

ACKNOWLEDGMENTS

We would like to thank Nikolay I. Shvetsov-Shilovski, Emilio Pisanty, Simon Brennecke, Xiaodan Mao and Kefei Wu as well as other researchers for their helpful discussions. This work was supported by the National Natural Science Foundation of China (Grant Nos. 92150105, 12474341, 12227807, and 12241407), the Science and Technology Commission of Shanghai Municipality (Grant Nos. 21ZR1420100 and 23JC1402000), and the Shanghai Pilot Program for Basic Research (Grant No. TQ20240204).

-
- [1] F. Krausz and M. Ivanov, Attosecond physics, *Rev. Mod. Phys.* **81**, 163 (2009).
 - [2] R. Pazourek, S. Nagele, and J. Burgdörfer, Attosecond chronoscopy of photoemission, *Rev. Mod. Phys.* **87**, 765 (2015).
 - [3] Y. Ma, H. Ni, and J. Wu, Attosecond ionization time delays in strong-field physics, *Chin. Phys. B* **33**, 13201 (2024).

- [4] P. Agostini, F. Fabre, G. Mainfray, G. Petite, and N. K. Rahman, Free-free transitions following six-photon ionization of xenon atoms, *Phys. Rev. Lett.* **42**, 1127 (1979).
- [5] T. F. Gallagher, Above-threshold ionization in low-frequency limit, *Phys. Rev. Lett.* **61**, 2304 (1988).
- [6] P. B. Corkum, N. H. Burnett, and F. Brunel, Above-threshold ionization in the long-wavelength limit, *Phys. Rev. Lett.* **62**, 1259 (1989).
- [7] L. V. Keldysh, Ionization in the field of a strong electromagnetic wave, *Sov. Phys. JETP* **20**, 1307 (1965).
- [8] M. Ammosov, N. Delone, and V. Krainov, Tunnel ionization of complex atoms and of atomic ions in an alternating electromagnetic field, *Sov. Phys. JETP* **64**, 1191 (1986).
- [9] N. B. Delone and V. P. Krainov, Tunneling and barrier-suppression ionization of atoms and ions in a laser radiation field, *Phys. Usp.* **41**, 469 (1998).
- [10] V. S. Popov, Tunnel and multiphoton ionization of atoms and ions in a strong laser field (keldysh theory), *Phys. Usp.* **47**, 855 (2004).
- [11] M. Y. Ivanov, M. Spanner, and O. Smirnova, Anatomy of strong field ionization, *J. Mod. Opt.* **52**, 165 (2005).
- [12] M. Ferray, A. L’Huillier, X. F. Li, L. A. Lompre, G. Mainfray, and C. Manus, Multiple-harmonic conversion of 1064 nm radiation in rare gases, *J. Phys. B: At. Mol. Opt. Phys.* **21**, L31 (1988).
- [13] A. L’Huillier, K. J. Schafer, and K. C. Kulander, Theoretical aspects of intense field harmonic generation, *J. Phys. B: At. Mol. Opt. Phys.* **24**, 3315 (1991).
- [14] J. L. Krause, K. J. Schafer, and K. C. Kulander, High-order harmonic generation from atoms and ions in the high intensity regime, *Phys. Rev. Lett.* **68**, 3535 (1992).
- [15] P. B. Corkum, Plasma perspective on strong field multiphoton ionization, *Phys. Rev. Lett.* **71**, 1994 (1993).
- [16] M. Lewenstein, Ph. Balcou, M. Yu. Ivanov, A. L’Huillier, and P. B. Corkum, Theory of high-harmonic generation by low-frequency laser fields, *Phys. Rev. A* **49**, 2117 (1994).
- [17] T. Popmintchev, M.-C. Chen, P. Arpin, M. M. Murnane, and H. C. Kapteyn, The attosecond nonlinear optics of bright coherent X-ray generation, *Nat. Photonics* **4**, 822 (2010).
- [18] B. Walker, B. Sheehy, L. F. DiMauro, P. Agostini, K. J. Schafer, and K. C. Kulander, Precision measurement of strong field double ionization of helium, *Phys. Rev. Lett.* **73**, 1227 (1994).
- [19] C. F. De Morisson Faria and X. Liu, Electron–electron correlation in strong laser fields, *J. Mod. Opt.* **58**, 1076 (2011).
- [20] D. Bauer and P. Koval, Qprop: A schrödinger-solver for intense laser–atom interaction, *Comput. Phys. Commun.* **174**, 396 (2006).
- [21] S. Patchkovskii and H. Muller, Simple, accurate, and efficient implementation of 1-electron atomic time-dependent Schrödinger equation in spherical coordinates, *Comput. Phys. Commun.* **199**, 153 (2016).
- [22] A. C. Brown, G. S. Armstrong, J. Benda, D. D. Clarke, J. Wragg, K. R. Hamilton, Z. Mašín, J. D. Gorfinkiel, and H. W. Van Der Hart, RMT: R-matrix with time-dependence. Solving the semi-relativistic, time-dependent schrödinger equation for general, multielectron atoms and molecules in intense, ultrashort, arbitrarily polarized laser pulses, *Comput. Phys. Commun.* **250**, 107062 (2020).
- [23] A. Scrinzi, tRecX — An environment for solving time-dependent Schrödinger-like problems, *Comput. Phys. Commun.* **270**, 108146 (2022).
- [24] Z.-H. Zhang, Y. Li, Y.-J. Mao, and F. He, QPC-TDSE: A parallel TDSE solver for atoms and small molecules in strong lasers, *Comput. Phys. Commun.* **290**, 108787 (2023).
- [25] S. V. Popruzhenko, Keldysh theory of strong field ionization: History, applications, difficulties and perspectives, *J. Phys. B: At. Mol. Opt. Phys.* **47**, 204001 (2014).
- [26] F. H. M. Faisal, Multiple absorption of laser photons by atoms, *J. Phys. B: At. Mol. Phys.* **6**, L89 (1973).
- [27] H. R. Reiss, Effect of an intense electromagnetic field on a weakly bound system, *Phys. Rev. A* **22**, 1786 (1980).
- [28] M. Bashkansky, P. H. Bucksbaum, and D. W. Schumacher, Asymmetries in above-threshold ionization, *Phys. Rev. Lett.* **60**, 2458 (1988).
- [29] S. Basile, F. Trombetta, and G. Ferrante, Twofold symmetric angular distributions in multiphoton ionization with elliptically polarized light, *Phys. Rev. Lett.* **61**, 2435 (1988).
- [30] P. Lambropoulos and X. Tang, Comment on “asymmetries in above-threshold ionization”, *Phys. Rev. Lett.* **61**, 2506 (1988).
- [31] H. G. Muller, G. Petite, and P. Agostini, Comment on “asymmetries in above-threshold ionization”, *Phys. Rev. Lett.* **61**, 2507 (1988).
- [32] P. Krstić and M. H. Mittleman, Angular distribution of electrons from multiphoton ionization by an elliptically polarized laser field, *Phys. Rev. A* **44**, 5938 (1991).
- [33] A. Jaroń, J. Kamiński, and F. Ehlotzky, Asymmetries in the angular distributions of above threshold ionization in an elliptically polarized laser field, *Opt. Commun.* **163**, 115 (1999).
- [34] S. P. Goreslavski, G. G. Paulus, S. V. Popruzhenko, and N. I. Shvetsov-Shilovski, Coulomb asymmetry in above-threshold ionization, *Phys. Rev. Lett.* **93**, 233002 (2004).

- [35] U. S. Sainadh, H. Xu, X. Wang, A. Atia-Tul-Noor, W. C. Wallace, N. Douguet, A. Bray, I. Ivanov, K. Bartschat, A. Kheifets, R. T. Sang, and I. V. Litvinyuk, Attosecond angular streaking and tunnelling time in atomic hydrogen, *Nature* **568**, 75 (2019).
- [36] R. Abrines and I. C. Percival, Classical theory of charge transfer and ionization of hydrogen atoms by protons, *Proc. Phys. Soc.* **88**, 861 (1966).
- [37] R. E. Olson and A. Salop, Charge-transfer and impact-ionization cross sections for fully and partially stripped positive ions colliding with atomic hydrogen, *Phys. Rev. A* **16**, 531 (1977).
- [38] B. Hu, J. Liu, and S.-g. Chen, Plateau in above-threshold-ionization spectra and chaotic behavior in rescattering processes, *Phys. Lett. A* **236**, 533 (1997).
- [39] T.-M. Yan, S. V. Popruzhenko, M. J. J. Vrakking, and D. Bauer, Low-energy structures in strong field ionization revealed by quantum orbits, *Phys. Rev. Lett.* **105**, 253002 (2010).
- [40] T.-M. Yan and D. Bauer, Sub-barrier coulomb effects on the interference pattern in tunneling-ionization photoelectron spectra, *Phys. Rev. A* **86**, 53403 (2012).
- [41] J.-W. Geng, L. Qin, M. Li, W.-H. Xiong, Y. Liu, Q. Gong, and L.-Y. Peng, Nonadiabatic tunneling ionization of atoms in elliptically polarized laser fields, *J. Phys. B: At. Mol. Opt. Phys.* **47**, 204027 (2014).
- [42] M. Li, J.-W. Geng, H. Liu, Y. Deng, C. Wu, L.-Y. Peng, Q. Gong, and Y. Liu, Classical-quantum correspondence for above-threshold ionization, *Phys. Rev. Lett.* **112**, 113002 (2014).
- [43] M. Li, X. Sun, X. Xie, Y. Shao, Y. Deng, C. Wu, Q. Gong, and Y. Liu, Revealing backward rescattering photoelectron interference of molecules in strong infrared laser fields, *Sci. Rep.* **5**, 8519 (2015).
- [44] M.-M. Liu, M. Li, C. Wu, Q. Gong, A. Staudte, and Y. Liu, Phase structure of strong-field tunneling wave packets from molecules, *Phys. Rev. Lett.* **116**, 163004 (2016).
- [45] N. I. Shvetsov-Shilovski, M. Lein, L. B. Madsen, E. Räsänen, C. Lemell, J. Burgdörfer, D. G. Arbó, and K. Tőkési, Semiclassical two-step model for strong-field ionization, *Phys. Rev. A* **94**, 13415 (2016).
- [46] N. I. Shvetsov-Shilovski, M. Lein, and L. B. Madsen, Multielectron polarization effects in strong-field ionization: Narrowing of momentum distributions and imprints in interference structures, *Phys. Rev. A* **98**, 23406 (2018).
- [47] N. I. Shvetsov-Shilovski and M. Lein, Semiclassical two-step model with quantum input: Quantum-classical approach to strong-field ionization, *Phys. Rev. A* **100**, 53411 (2019).
- [48] N. I. Shvetsov-Shilovski, M. Lein, and K. Tőkési, Semiclassical two-step model for ionization of the hydrogen molecule by a strong laser field, *Eur. Phys. J. D* **73**, 37 (2019).
- [49] S. Brennecke, N. Eicke, and M. Lein, Gouy’s phase anomaly in electron waves produced by strong-field ionization, *Phys. Rev. Lett.* **124**, 153202 (2020).
- [50] N. I. Shvetsov-Shilovski, Semiclassical two-step model for ionization by a strong laser pulse: Further developments and applications, *Eur. Phys. J. D* **75**, 130 (2021).
- [51] X.-Y. Lai, C. Poli, H. Schomerus, and C. F. D. M. Faria, Influence of the coulomb potential on above-threshold ionization: A quantum-orbit analysis beyond the strong-field approximation, *Phys. Rev. A* **92**, 43407 (2015).
- [52] A. S. Maxwell, A. Al-Jawahiry, T. Das, and C. F. D. M. Faria, Coulomb-corrected quantum interference in above-threshold ionization: Working towards multitrajectory electron holography, *Phys. Rev. A* **96**, 23420 (2017).
- [53] A. S. Maxwell, A. Al-Jawahiry, X. Y. Lai, and C. Figueira De Morisson Faria, Analytic quantum-interference conditions in coulomb corrected photoelectron holography, *J. Phys. B: At. Mol. Opt. Phys.* **51**, 44004 (2018).
- [54] A. S. Maxwell and C. F. De Morisson Faria, Coulomb-free and coulomb-distorted recolliding quantum orbits in photoelectron holography, *J. Phys. B: At. Mol. Opt. Phys.* **51**, 124001 (2018).
- [55] A. S. Maxwell, S. V. Popruzhenko, and C. F. D. M. Faria, Treating branch cuts in quantum trajectory models for photoelectron holography, *Phys. Rev. A* **98**, 63423 (2018).
- [56] M. B. Carlsen, E. Hansen, L. B. Madsen, and A. S. Maxwell, Advanced momentum sampling and maslov phases for a precise semiclassical model of strong-field ionization, *New J. Phys.* **26**, 23025 (2024).
- [57] In this paper, we use \mathbf{k} to denote the momentum/velocity of the electron when the laser is on, to distinguish it from the canonical momentum $\mathbf{p} = \mathbf{k} - \mathbf{A}$. After the laser turned off, we have $\mathbf{p} = \mathbf{k}$.
- [58] A. Perelomov, V. Popov, and M. Terent’ev, Ionization of atoms in an alternating electric field, *Sov. Phys. JETP* **23**, 924 (1966).
- [59] D. R. Hartree, The wave mechanics of an atom with a non-coulomb central field. Part I. Theory and methods, *Math. Proc. Cambridge Philos. Soc.* **24**, 89 (1928).
- [60] Here k is actually $\sqrt{\mathbf{k} \cdot \mathbf{k}}$ and is not the conventional “norm” of the complex vector, which is $\|\mathbf{k}\| = \sqrt{\mathbf{k}^* \cdot \mathbf{k}}$. Here we normalize the complex vector \mathbf{k} through $\hat{\mathbf{k}} = \mathbf{k}/\sqrt{\mathbf{k} \cdot \mathbf{k}}$, according to Ref. [58].
- [61] E. Pisanty and Á. Jiménez-Galán, Strong-field approximation in a rotating frame: High-order harmonic emission from p states in bicircular fields, *Phys. Rev. A* **96**, 63401 (2017).

- [62] The evaluation of spherical harmonic in the complex domain makes use of the fact that the solid harmonics $S_{lm}(\mathbf{r}) := r^l Y_{lm}(\hat{\mathbf{r}})$ can be expressed in a polynomial of x, y, z , see Ref. [103].
- [63] G. F. Gribakin and M. Yu. Kuchiev, Multiphoton detachment of electrons from negative ions, *Phys. Rev. A* **55**, 3760 (1997).
- [64] H. Ni, N. Eicke, C. Ruiz, J. Cai, F. Oppermann, N. I. Shvetsov-Shilovski, and L.-W. Pi, Tunneling criteria and a nonadiabatic term for strong-field ionization, *Phys. Rev. A* **98**, 13411 (2018).
- [65] H. Ni, S. Brennecke, X. Gao, P.-L. He, S. Donsa, I. Březinová, F. He, J. Wu, M. Lein, X.-M. Tong, and J. Burgdörfer, Theory of Subcycle Linear Momentum Transfer in Strong-Field Tunneling Ionization, *Phys. Rev. Lett.* **125**, 073202 (2020).
- [66] X. Mao, H. Ni, X. Gong, J. Burgdörfer, and J. Wu, Subcycle-resolved strong-field tunneling ionization: Identification of magnetic dipole and electric quadrupole effects, *Phys. Rev. A* **106**, 63105 (2022).
- [67] Y. Ma, J. Zhou, P. Lu, H. Ni, and J. Wu, Influence of nonadiabatic, nondipole and quantum effects on the attoclock signal, *J. Phys. B: At. Mol. Opt. Phys.* **54**, 144001 (2021).
- [68] Y. Ma, H. Ni, Y. Li, F. He, and J. Wu, Subcycle conservation law in strong-field ionization, *Ultrafast Sci.* **4**, 0071 (2024).
- [69] J. Muth-Böhm, A. Becker, and F. H. M. Faisal, Suppressed molecular ionization for a class of diatomics in intense femtosecond laser fields, *Phys. Rev. Lett.* **85**, 2280 (2000).
- [70] X. M. Tong, Z. X. Zhao, and C. D. Lin, Theory of molecular tunneling ionization, *Phys. Rev. A* **66**, 33402 (2002).
- [71] T. K. Kjeldsen and L. B. Madsen, Strong-field ionization of N_2 : Length and velocity gauge strong-field approximation and tunnelling theory, *J. Phys. B: At. Mol. Opt. Phys.* **37**, 2033 (2004).
- [72] T. K. Kjeldsen, C. Z. Bisgaard, L. B. Madsen, and H. Stapelfeldt, Influence of molecular symmetry on strong-field ionization: Studies on ethylene, benzene, fluorobenzene, and chlorofluorobenzene, *Phys. Rev. A* **71**, 13418 (2005).
- [73] M. Born and R. Oppenheimer, Zur quantentheorie der molekeln, *Ann. Phys.* **389**, 457 (1927).
- [74] O. I. Tolstikhin, T. Morishita, and L. B. Madsen, Theory of tunneling ionization of molecules: Weak-field asymptotics including dipole effects, *Phys. Rev. A* **84**, 53423 (2011).
- [75] L. B. Madsen, F. Jensen, O. I. Tolstikhin, and T. Morishita, Structure factors for tunneling ionization rates of molecules, *Phys. Rev. A* **87**, 13406 (2013).
- [76] O. I. Tolstikhin, L. B. Madsen, and T. Morishita, Weak-field asymptotic theory of tunneling ionization in many-electron atomic and molecular systems, *Phys. Rev. A* **89**, 13421 (2014).
- [77] R. Saito, O. I. Tolstikhin, L. B. Madsen, and T. Morishita, Structure factors for tunneling ionization rates of diatomic molecules, *At. Data Nucl. Data Tables* **103–104**, 4 (2015).
- [78] V. H. Trinh, V. N. T. Pham, O. I. Tolstikhin, and T. Morishita, Weak-field asymptotic theory of tunneling ionization including the first-order correction terms: Application to molecules, *Phys. Rev. A* **91**, 63410 (2015).
- [79] A. I. Dnestryan and O. I. Tolstikhin, Integral-equation approach to the weak-field asymptotic theory of tunneling ionization, *Phys. Rev. A* **93**, 33412 (2016).
- [80] L. B. Madsen, F. Jensen, A. I. Dnestryan, and O. I. Tolstikhin, Structure factors for tunneling ionization rates of molecules: General hartree-fock-based integral representation, *Phys. Rev. A* **96**, 13423 (2017).
- [81] A. I. Dnestryan, O. I. Tolstikhin, L. B. Madsen, and F. Jensen, Structure factors for tunneling ionization rates of molecules: General grid-based methodology and convergence studies, *J. Chem. Phys.* **149**, 164107 (2018).
- [82] S. Song, M. Zhu, H. Ni, and J. Wu, PyStructureFactor: A python code for the molecular structure factor in tunneling ionization rates, *Comput. Phys. Commun.* **292**, 108882 (2023).
- [83] N. I. Shvetsov-Shilovski, D. Dimitrovski, and L. B. Madsen, Ionization in elliptically polarized pulses: Multielectron polarization effects and asymmetry of photoelectron momentum distributions, *Phys. Rev. A* **85**, 023428 (2012).
- [84] Currently, available units include: (1) length pm, Å, nm, µm, cm, mm and m; (2) time as, fs, ps and ns; (3) energy eV; (4) power W, GW, TW and PW; (5) angle rad and ° (deg). Other units are also available by importing the `Unitful.jl` package.
- [85] In the Julia REPL, the `vscode` with the `julia extension` installed, or the `vim` editor with the `julia-vim` extension installed, the user may type special Unicode characters in a LaTeX-like manner. For example, the degree symbol is typed in such way: “`\degree`”, where “`↵`” indicates the TAB key.
- [86] X. M. Tong and C. D. Lin, Empirical formula for static field ionization rates of atoms and molecules by lasers in the barrier-suppression regime, *J. Phys. B: At. Mol. Opt. Phys.* **38**, 2593 (2005).
- [87] Q. Sun, T. C. Berkelbach, N. S. Blunt, G. H. Booth, S. Guo, Z. Li, J. Liu, J. D. McClain, E. R. Sayfutyarova, S. Sharma, S. Wouters, and G. K.-L. Chan, PySCF: The python-based simulations of chemistry framework, *WIREs Comput. Mol. Sci.* **8**, e1340 (2018).
- [88] C. Rackauckas and Q. Nie, DifferentialEquations.jl – a performant and feature-rich ecosystem for solving differential equations in julia, *J. Open Res. Software* **5**, 15 (2017).
- [89] D. G. Arbó, S. Yoshida, E. Persson, K. I. Dimitriou, and J. Burgdörfer, Interference oscillations in the angular distribution of laser-ionized electrons near ionization threshold, *Phys. Rev. Lett.* **96**, 143003 (2006).

- [90] D. G. Arbó, K. I. Dimitriou, E. Persson, and J. Burgdörfer, Sub-poissonian angular momentum distribution near threshold in atomic ionization by short laser pulses, *Phys. Rev. A* **78**, 013406 (2008).
- [91] S. De, I. Znakovskaya, D. Ray, F. Anis, N. G. Johnson, I. A. Bocharova, M. Magrakvelidze, B. D. Esry, C. L. Cocke, I. V. Litvinyuk, and M. F. Kling, Field-free orientation of CO molecules by femtosecond two-color laser fields, *Phys. Rev. Lett.* **103**, 153002 (2009).
- [92] X. Gong, P. He, Q. Song, Q. Ji, H. Pan, J. Ding, F. He, H. Zeng, and J. Wu, Two-dimensional directional proton emission in dissociative ionization of H₂, *Phys. Rev. Lett.* **113**, 203001 (2014).
- [93] K. Lin, X. Jia, Z. Yu, F. He, J. Ma, H. Li, X. Gong, Q. Song, Q. Ji, W. Zhang, H. Li, P. Lu, H. Zeng, J. Chen, and J. Wu, Comparison study of strong-field ionization of molecules and atoms by bicircular two-color femtosecond laser pulses, *Phys. Rev. Lett.* **119**, 203202 (2017).
- [94] P. V. Demekhin, A. N. Artemyev, A. Kastner, and T. Baumert, Photoelectron circular dichroism with two overlapping laser pulses of carrier frequencies ω and 2ω linearly polarized in two mutually orthogonal directions, *Phys. Rev. Lett.* **121**, 253201 (2018).
- [95] H. Li, X. Gong, H. Ni, P. Lu, X. Luo, J. Wen, Y. Yang, X. Qian, Z. Sun, and J. Wu, Light-induced ultrafast molecular dynamics: From photochemistry to optochemistry, *J. Phys. Chem. Lett.* **13**, 5881 (2022).
- [96] W. Humphrey, A. Dalke, and K. Schulten, VMD: Visual molecular dynamics, *J. Mol. Graphics* **14**, 33 (1996).
- [97] F. W. J. Olver, D. W. Lozier, R. F. Boisvert, and C. W. Clark, eds., *The NIST Handbook of Mathematical Functions* (Cambridge University Press, 2010).
- [98] B. M. Smirnov and M. I. Chibisov, The breaking up of atomic particles by an electric field and by electron collisions, *Sov. Phys. JETP* **22**, 585 (1966).
- [99] C. Z. Bisgaard and L. B. Madsen, Tunneling ionization of atoms, *Am. J. Phys.* **72**, 249 (2004).
- [100] A. Perelomov and V. Popov, Ionization of atoms in an alternating electrical field. III, *Sov. Phys. JETP* **25**, 336 (1967).
- [101] S. Popruzhenko and D. Bauer, Strong field approximation for systems with coulomb interaction, *J. Mod. Opt.* **55**, 2573 (2008).
- [102] S. V. Popruzhenko, V. D. Mur, V. S. Popov, and D. Bauer, Strong field ionization rate for arbitrary laser frequencies, *Phys. Rev. Lett.* **101**, 193003 (2008).
- [103] M. J. Caola, Solid harmonics and their addition theorems, *J. Phys. A: Math. Gen.* **11**, L23 (1978).